
Neural Galerkin Normalizing Flows for Bayesian Inference of Diffusions with Inaccessible Boundaries

Riccardo Saporiti
CSQI

École Polytechnique Fédérale de Lausanne
Lausanne, Switzerland 1015
riccardo.saporiti@epfl.ch

Fabio Nobile
CSQI

École Polytechnique Fédérale de Lausanne
Lausanne, Switzerland 1015
fabio.nobile@epfl.ch

Abstract

One of the primary challenges in Bayesian inference on the parameters of a diffusion model from discrete observations is the unavailability of an analytical expression for the transition density function between consecutive observation times, which is needed to derive the likelihood function.

Extending previous studies that solve Fokker-Planck (FP) type partial differential equations with Normalizing Flows, we propose a new Normalizing Flow architecture to learn the transition density function of the diffusion process between two observation times. We do so by solving in a Neural Galerkin framework the associated FP equation with a Dirac mass as initial condition, over a specified training distribution of the initial datum and the coefficients of the diffusion. We specifically focus on processes whose diffusion matrix vanishes in certain inaccessible boundary regions, such as Stochastic Volatility models that satisfy a Feller condition.

The product of the obtained transition densities evaluated along the observed trajectory approximates the likelihood function, thereby enabling cheap posterior sampling via Markov chain Monte Carlo (MCMC). After the offline training phase, inference becomes significantly more efficient, as it avoids the need to solve the FP equation in real time for each parameter proposed by the MCMC sampler or to rely on other likelihood-free methods for Bayesian inference that involve repeated simulation of diffusion bridges.

1 Introduction

One of the most challenging aspects of performing Bayesian Inference on the parameters of discretely observed diffusion processes is the unavailability of an analytic expression of the likelihood function. This limitation has spurred research to develop positive estimators for the likelihood function through numerical integration of the diffusion process or exact simulation techniques [1, 2]. However, exact simulation of diffusion processes between two observed values is notoriously difficult, especially for nonlinear, multivariate Stochastic Differential Equations (SDEs). In many cases, it is necessary to use numerical discretization by adding imputed points between two observation time instants [3, 4]. Depending on the focus of the inference, either Metropolis-within-Gibbs, Pseudo-Marginal MCMC, or Particle MCMC algorithms are usually employed [5, 6, 7]. These approaches quickly become very costly, particularly in low-frequency observation regimes, where many imputed points are needed, potentially leading to unwanted correlations in the chain [8].

A less explored direction is to seek an explicit approximation of the Transition Probability Density Function (TPDF) between two observations. Such a TPDF is the solution of the well-known Fokker-Planck (FP) partial differential equation (PDE) [9]. This equation poses significant numerical

challenges due to positivity and integrability constraints, and because its initial condition is a Dirac delta distribution, which is difficult to approximate numerically.

Since the likelihood of a trajectory composed of $n + 1$ discrete observations factors into the product of n TPDFs, the computational cost for a single likelihood evaluation grows with the length of the time series. This computational burden must be incurred for each sample generated by an MCMC-type algorithm that walks towards the posterior distribution of the SDE parameters given the data. Therefore, developing efficient numerical algorithms for fast likelihood evaluation is vital for several real-time applications.

Nowadays, Deep Learning algorithms have enabled the solution of (parametric) PDEs that are intractable for traditional discretization methods [10, 11, 12, 13, 14]. However, the use of Deep Learning for transition density estimation is still in its early stages. In [15], Physics-Informed Neural Networks (PINNs) are used to compute parametric approximations of the Kolmogorov Backward equation that solves for the cumulative density function. This method does not ensure that the numerical solution represents a valid density function, which could limit its applicability in Bayesian inference for diffusion processes.

Normalizing Flows (NFs) have demonstrated promising results in solving FP equations within data-driven frameworks [16] and alongside PINN-based approaches [17, 18]. Nonetheless, PINNs, which train a neural network uniformly in the space-time domain, struggle to enforce the causality of the numerical solution and are notoriously prone to failure in advection-dominated regimes [19, 20]. In this context, concentrated initial conditions further complicate the issue by contributing to the emergence of highly spatially localized features in the solution.

To approximate TPDFs associated with FP equations with no boundaries, the work [21] used NFs combined with the Neural Galerkin framework of [22], yielding Neural Galerkin Normalizing Flows (NGNFs). The authors proposed using real-valued non-volume preserving transformations to approximate the TPDF parametrically with respect to the position of the Dirac delta initial condition. In contrast to traditional PINNs, NGNFs avoid solving the PDE over the entire space-time domain and, through an adaptive sampling strategy, propagate the NF’s parameters forward in time, naturally preserving causality.

In this work, we follow a similar path but consider a different NF architecture that can accommodate inaccessible boundaries. Moreover, we propose a Bayesian inference methodology based on NGNF to infer the parameters of the SDE, and validate it on Stochastic Volatility (SV) models, a class of non-uniformly elliptic diffusion processes linked to an advection-dominated FP equation that poses significant challenges for traditional numerical solvers.

1.1 Existing methodologies for Bayesian inference of diffusion processes

Since the TPDF is generally unavailable, the literature has proposed several alternatives for Bayesian Inference, including a) discretization-based MCMC [8, 23, 24, 25], b) exact simulation [1, 2, 26, 27], c) likelihood-free methods [28, 29], d) variational inference [30] and e) closed-form expansions [31, 32, 33, 34]. While these approaches can be effective for specific applications, they also present certain drawbacks. These may include high online computational costs (a, b, c), bias associated with discretization of the SDE (a, c, d), or limited applicability (b, e), underscoring the need for scalable likelihood surrogates.

1.2 Contributions

- We build on the NGNF framework developed in [21] and introduce a new class of bounded Normalizing Flows to solve parametric FP equations with vanishing diffusion at inaccessible boundaries. This approach effectively addresses advection-dominated PDEs. The NF is parameterized by the SDE parameters and the position of the initial Dirac mass to enable statistical inference.
- Unlike purely data-driven methods, such as those based on learning the NF from forward simulation of the SDE, our approach more strongly enforces the structural properties of a flow of probability measures and, thanks to adaptive sampling schemes, allows for coherent modeling of the relationships among the diffusion parameters, the initial condition, and the final solution.

- We propose a Bayesian inference procedure based on our NGNFs and evaluate its performance on fully observed SV models. Our results show that NFs enable fast likelihood evaluation and robustness in low-frequency observation regimes, thereby considerably accelerating Bayesian inference for diffusion models.

2 Problem Formulation

Let $\mathbf{X}(t)$ be a d -dimensional stochastic process satisfying an SDE of the form

$$d\mathbf{X}(t) = \mathbf{b}(t, \mathbf{X}(t), \boldsymbol{\mu})dt + \sqrt{\Sigma(t, \mathbf{X}(t), \boldsymbol{\mu})}d\mathbf{W}(t) \quad \text{for } t \in (0, T], \quad (1)$$

where $T > 0$, $\mathbf{b} : [0, T] \times \Omega \times \Xi \rightarrow \mathbb{R}^d$ is a drift function, $\Sigma : [0, T] \times \Omega \times \Xi \rightarrow \mathbb{R}^{d \times d}$ is a semi-positive definite matrix, $\boldsymbol{\mu} \in \Xi \subset \mathbb{R}^p$ is a p dimensional vector of parameters, $\mathbf{W}(t)$ is a d -dimensional vector of uncorrelated Brownian Motions and $\Omega \subseteq \mathbb{R}^d$ is the domain of $\mathbf{X}(t)$. We assume that the domain of the diffusion process is of the form:

$$\Omega = \{\mathbf{x} \in \mathbb{R}^d : a_m < x_m \quad \text{for } m = 1, \dots, d\}, \quad (2)$$

where $a_m \in \mathbb{R} \cup \{-\infty\}$, and the diffusion matrix Σ degenerates on $\partial\Omega$. This condition is typical of SV models, where the volatility of the asset is the state variable that drives the determinant of the diffusion matrix to zero.

Let $T > t > s \geq 0$. The transition probability density function (TPDF) of $\mathbf{X}(t)|\mathbf{X}(s) = \mathbf{x}_0 \in \Omega$ is denoted by $\rho(\mathbf{x}|t, s, \mathbf{x}_0)$ and satisfies $\mathbb{P}(\mathbf{X}(t) \in A | \mathbf{X}(s) = \mathbf{x}_0) = \int_A \rho(\mathbf{x}|t, s, \mathbf{x}_0)d\mathbf{x}$ for any Borel set $A \subset \Omega$. It is well-known that the TPDF evolves according to the Fokker-Planck equation [9]

$$\left\{ \begin{array}{ll} \partial_t \rho(\mathbf{x}|t, s, \mathbf{x}_0, \boldsymbol{\mu}) = \mathcal{L}_t^* (\rho(\cdot|t, s, \mathbf{x}_0, \boldsymbol{\mu})) (\mathbf{x}) & \text{for } \mathbf{x} \in \Omega, t \in (s, T], \quad (3a) \\ \rho(\mathbf{x}|s, s, \mathbf{x}_0, \boldsymbol{\mu}) = \delta_{\mathbf{x}_0}(\mathbf{x}) & \text{for } \mathbf{x} \in \Omega, \quad (3b) \\ \int_{\Omega} \rho(\mathbf{x}|t, s, \mathbf{x}_0, \boldsymbol{\mu}) d\mathbf{x} = 1 & \text{for } t \in (s, T], \quad (3c) \\ \rho(\mathbf{x}|t, s, \mathbf{x}_0, \boldsymbol{\mu}) \geq 0 & \text{for } \mathbf{x} \in \Omega, t \in (s, T], \quad (3d) \end{array} \right.$$

where $\delta_{\mathbf{y}}(\cdot)$ denotes the Dirac delta distribution centered at $\mathbf{y} \in \mathbb{R}^d$ and \mathcal{L}^* is the L^2 adjoint of the generator of the Markov Process $\mathbf{X}(t)$, which reads, for $f \in \mathcal{C}^2(\Omega; \mathbb{R})$

$$\mathcal{L}_t^*(f(\cdot))(\mathbf{x}) = \nabla_{\mathbf{x}} \cdot [-\mathbf{b}(t, \mathbf{x}, \boldsymbol{\mu})f(\mathbf{x}) + \frac{1}{2}\nabla_{\mathbf{x}} \cdot (\Sigma(t, \mathbf{x}, \boldsymbol{\mu})f(\mathbf{x}))], \quad (4)$$

see e.g. [35]. In this work, we focus on the case where the boundary $\partial\Omega$ is inaccessible, and we specifically treat SV models that satisfy a strict Feller condition. Under these assumptions, the solution $\rho(\cdot|t, s, \mathbf{x}_0, \boldsymbol{\mu})$ is identically zero on $\partial\Omega$, leading to a boundary condition of homogeneous Dirichlet type [36, 37].

3 Nonlinear parametrization of the Transition Probability Density Function

Normalizing Flows are diffeomorphisms that transform the probability density function (PDF) of a source distribution into that of a target distribution, often using parameterizations based on neural networks. Following the Neural Galerkin framework, we represent the approximated solution of the FP PDE at a specific time t by the time-dependent vector of parameters $\boldsymbol{\theta}(\tau) \in \Theta \subseteq \mathbb{R}^M$ that characterizes the architecture of the employed Normalizing Flow, namely

$$\rho(\mathbf{x}|t, s, \mathbf{x}_0, \boldsymbol{\mu}) \simeq P(\mathbf{x}|\boldsymbol{\theta}(\tau), s, \mathbf{x}_0, \boldsymbol{\mu}), \quad (5)$$

where $\tau = t - s$, and P represents the PDF (parametric in $s, \mathbf{x}_0, \boldsymbol{\mu}$) generated by the Normalizing Flow with parameter vector $\boldsymbol{\theta}(\tau)$. For further details, see section 4.

We assume that the observations of the stochastic process (1) are collected within the time interval $[0, T]$. For a fixed $s \in [0, T - \Delta]$, we solve the FP PDE over the time horizon $[s, s + \Delta]$, where $\Delta > 0$ represents the maximum time between observations. In turn, this implies that $\tau \in [0, \Delta]$. For convenience, we incorporate s into the vector $\boldsymbol{\mu}$, defining $\tilde{\boldsymbol{\mu}} = [\boldsymbol{\mu}, s] \in \Xi^* = \Xi \times [0, T - \Delta] \subseteq \mathbb{R}^{p+1}$. Hence, the NF's PDF (5) is rewritten as $P(\mathbf{x}|\boldsymbol{\theta}(\tau), \mathbf{x}_0, \tilde{\boldsymbol{\mu}})$.

3.1 System of ODEs for Normalizing Flow's parameters

Following the approach outlined in [22, 21], we extend the derivation of the system of ODEs describing the time evolution of the parameters $\boldsymbol{\theta}(\tau)$ to the $\tilde{\boldsymbol{\mu}}$ -parametric setting. We substitute the ansatz (5) into the PDE for the TPDF (3). Assuming that $\boldsymbol{\theta}(\tau)$ is differentiable, we obtain the residual function $r_{t,s} : \Theta \times \dot{\Theta} \times \Omega \times \Omega \times \Xi^* \rightarrow \mathbb{R}$ defined as

$$r_{t,s}(\boldsymbol{\theta}, \boldsymbol{\zeta}, \mathbf{x}, \mathbf{x}_0, \tilde{\boldsymbol{\mu}}) = \nabla_{\boldsymbol{\theta}} P(\mathbf{x}|\boldsymbol{\theta}(\tau), \mathbf{x}_0, \tilde{\boldsymbol{\mu}}) \cdot \boldsymbol{\zeta} - \mathcal{L}_t^*(P(\cdot|\boldsymbol{\theta}(\tau), \mathbf{x}_0, \tilde{\boldsymbol{\mu}}))(\mathbf{x}), \quad (6)$$

where $\dot{\Theta}$ is the set of time derivatives of $\boldsymbol{\theta}$. The evolution of the parameters of the Normalizing Flow is given by the following optimization problem, which has to be solved at each time instant:

$$\dot{\boldsymbol{\theta}}(\tau) \in \arg \min_{\boldsymbol{\zeta} \in \dot{\Theta}} J_{\tau}(\boldsymbol{\theta}, \boldsymbol{\zeta}), \quad (7)$$

where the objective $J_{\tau} : \Theta \times \dot{\Theta} \rightarrow \mathbb{R}$ is defined as

$$J_{\tau}(\boldsymbol{\theta}, \boldsymbol{\zeta}) = \int_{\Xi^*} \int_{\Omega} \int_{\Omega} |r_{s+\tau,s}(\boldsymbol{\theta}, \boldsymbol{\zeta}, \mathbf{x}, \mathbf{x}_0, \tilde{\boldsymbol{\mu}})|^2 d\nu_{\boldsymbol{\theta}(\tau)}(\mathbf{x}|\mathbf{x}_0, \tilde{\boldsymbol{\mu}}) d\eta(\mathbf{x}_0) d\tilde{\pi}_0^*(\tilde{\boldsymbol{\mu}}). \quad (8)$$

In (8), η and $\nu_{\boldsymbol{\theta}(\tau)}$ are positive measures over $\hat{\Omega} \subseteq \Omega$, where $\hat{\Omega}$ is the support of the PDFs generated by the NF, which will be specified later. $\tilde{\pi}_0^*$ denotes the joint distribution that tensorizes a distribution over the parameters of the SDE (1), denoted as $\tilde{\pi}_0$, with the uniform distribution $\mathcal{U}(\cdot; [0, T - \Delta])$. Thanks to the properties of the map defined by the Normalizing Flow at time t , we can sample progressively from the evolving approximation P , which allows us to take $\nu_{\boldsymbol{\theta}(\tau)}(\cdot|\cdot, \cdot) = P(\cdot|\boldsymbol{\theta}(\tau), \cdot, \cdot)$. Similar choices are employed in [22, 21] and are crucial for tackling the curse of dimensionality in advection-dominated PDEs. Numerically, (8) is approximated by Monte Carlo sampling, resulting in a least squares problem that is solved by using LSMR [38].

4 Normalizing Flow for Transition Density Estimation

4.1 Background on Normalizing Flows

NFs are bijective, differentiable transformations $\mathbf{n}_{\boldsymbol{\theta}} : \mathcal{X} \rightarrow \mathcal{Z}$ used to relate the PDF of a target random variable $\mathbf{X} \in \mathcal{X} \subseteq \mathbb{R}^d$ to that of a source (reference) random variable $\mathbf{Z} \in \mathcal{Z} \subseteq \mathbb{R}^d$. For a given set of parameters $\boldsymbol{\theta} \in \Theta \subseteq \mathbb{R}^M$, the density of the target random variable is expressed through the change of variables formula

$$p_{\mathbf{X}}(\mathbf{x}) = p_{\mathbf{Z}}(\mathbf{n}_{\boldsymbol{\theta}}(\mathbf{x})) |\det(\nabla_{\mathbf{x}} \mathbf{n}_{\boldsymbol{\theta}}(\mathbf{x}))|, \quad (9)$$

where $p_{\mathbf{X}}$ and $p_{\mathbf{Z}}$ are the PDFs of \mathbf{X} and \mathbf{Z} respectively.

According to this formula, we can obtain samples from \mathbf{X} by mapping back samples from the reference distribution $\mathbf{z} \sim \mathbf{Z}$ through the Flow, such that $\mathbf{x} = \mathbf{n}_{\boldsymbol{\theta}}^{-1}(\mathbf{z})$.

In this work, we utilize the identity given by the change of variable formula (9) to represent the solution of the FP equation. This immediately ensures that the numerical solution satisfies the properties described in (3c), (3d).

We work under the following assumption: the target TPDF decays at infinity more rapidly than any polynomial. This assumption is reasonable for SDEs with coefficients that grow at most linearly at infinity and allows us to approximate the TPDF using a Normalizing Flow with compact support. Therefore, we confine the TPDF realized by the NF to the hyperrectangle $\hat{\Omega} = \bigotimes_{m=1}^d (\hat{a}_m, \hat{b}_m)$, where $\hat{\mathbf{a}}, \hat{\mathbf{b}} \in \mathbb{R}^d$ and $-\hat{a}_m, \hat{b}_m$ are large enough for all $m \in \{1, \dots, d\}$ except those for which $a_m > -\infty$ (cf. equation (2)), where we set $\hat{a}_m = a_m$. With this construction, $\partial \hat{\Omega}$ contains a portion of the true boundary of the state space, namely $\Gamma = \partial \Omega \cap \partial \hat{\Omega} \neq \emptyset$. We solve the FP PDE on $\hat{\Omega}$ by imposing homogeneous Dirichlet boundary conditions on Γ and zero-flux boundary conditions, corresponding to reflected diffusion, on the artificial boundary $\partial \hat{\Omega} \setminus \Gamma$.

4.2 Truncated-Gaussian Normalizing Flows for probability density estimation

For a fixed $\tau > 0$, the source distribution $p_{\mathbf{Z}}$ is transformed through a time-dependent mapping, defining an approximation to the TPDF that solves (3) as

$$P(\mathbf{x}|\boldsymbol{\theta}(\tau), \mathbf{x}_0, \tilde{\boldsymbol{\mu}}) = p_{\mathbf{Z}}(\mathbf{n}_{\boldsymbol{\theta}(\tau)}(\mathbf{x}|\mathbf{x}_0, \tilde{\boldsymbol{\mu}})) |\det(\nabla_{\mathbf{x}} \mathbf{n}_{\boldsymbol{\theta}(\tau)}(\mathbf{x}|\mathbf{x}_0, \tilde{\boldsymbol{\mu}}))|. \quad (10)$$

Our architecture models the mapping $\mathbf{n}_{\theta(\tau)}$ by stacking several bijections in sequence. The final transformation builds upon the composition of an integer number of layers, $L \geq 1$, such that, for $m = 0, \dots, d - 1$

$$\begin{cases} (\mathbf{n}_{\theta(\tau)}(\mathbf{x}|\mathbf{x}_0, \tilde{\boldsymbol{\mu}}))_{m+1} = x_{m+1}^L \\ x_{m+1}^l = n_{\theta^l(\tau)}^{l,m+1}(x_{m+1}^{l-1}|\mathbf{x}_{1:m}^1, \mathbf{x}_0, \tilde{\boldsymbol{\mu}}) \quad \text{for } l = 1, \dots, L \\ x_{m+1}^0 = x_{m+1}, \end{cases} \quad (11)$$

where $\mathbf{x}_{1:0}^1 = \emptyset$.

The smooth, bounded Normalizing Flow is characterized by a nonlinear invertible mapping which, after rescaling $\widehat{\Omega}$ to $[-1, 1]^d$, we recursively apply for $l = 2, \dots, L$ and for $m = 0, \dots, d - 1$. We define the mapping using the cumulative density function (CDF) of a mixture of truncated Gaussians (MTG) random variables

$$\tilde{F} : [-1, 1] \rightarrow [-1, 1], \quad \tilde{F}(x) = 2 \left[\sum_{k=1}^G \alpha_k \Phi_{[-1,1]}(x|\mathbf{m}_k, \sigma_k) \right] - 1, \quad (12)$$

where $\Phi_{[x,y]}(\cdot|m, \sigma)$ and $\phi_{[x,y]}(\cdot|m, \sigma)$ denote the CDF and PDF, respectively, of a Gaussian random variable truncated to the interval $[x, y]$, with m and σ representing the mean and standard deviation of the parent Normal distribution [39].

Transformation (11) involves an affine rescaling followed by $L - 1$ applications of (12) to a one-dimensional input vector while conditioning on the other state variables. The first layer maps the NF's support to the unit-hypercube $[-1, 1]^d$. In formulas, for $m = 0, \dots, d - 1$,

$$n_{\theta^1(\tau)}^{1,m+1}(x_{m+1}^1|\mathbf{x}_{1:m}^1, \mathbf{x}_0, \boldsymbol{\mu}) = 2 \frac{x_{m+1}^1 - \hat{a}_{m+1}}{\hat{b}_{m+1} - \hat{a}_{m+1}} - 1. \quad (13)$$

The conditioning variable \mathbf{x}_0 is also processed by (13).

The dependency of the mapping on the parameters of (1), the location of the initial condition (3), and the observation time s is introduced through $d(L - 1)$ Neural Networks; one for every layer $l = 2, \dots, L$ of the d conditioned transformations. The mean, variance, and mixture weights of each Gaussian in (12) are the output of the Neural Network of the corresponding layer. For each $m = 1, \dots, d$, the m -th Gaussian mixture at level l contains $G_{l,m} > 0$ elements. Consequently, the corresponding Neural Network takes an input in dimension $m + d + p + 1$ and outputs a $3 \times G_{l,m}$ dimensional vector. Softmax activation functions ensure that the mixture weights sum to 1. In equation form:

$$[\boldsymbol{\alpha}^{l,m+1}; \mathbf{m}^{l,m+1}; \boldsymbol{\sigma}^{l,m+1}] = \text{NN}_{\theta^{l,m+1}(\tau)}^{l,m+1}(\mathbf{x}_{1:m}^1, \mathbf{x}_0, \tilde{\boldsymbol{\mu}}), \quad \text{for } m = 0, \dots, d - 1, \text{ and } l = 2, \dots, L, \quad (14)$$

where $\text{NN}_{\theta^{l,m+1}(\tau)}^{l,m+1}$ is a Neural Network with parameters $\theta^{l,m+1}$. The architecture of these Neural Networks is based upon GRU cells, which are particularly effective for modeling solutions to PDEs that display sharp transitions in the initial conditions [11]. With these ingredients, we define the bijection from $[-1, 1]^d$ to $[-1, 1]^d$ applied at layer $l = 2, \dots, L$ and for $m = 0, \dots, d - 1$

$$\begin{aligned} x_{m+1}^l &= n_{\theta^l(\tau)}^{l,m+1}(x_{m+1}^{l-1}|\mathbf{x}_{1:m}^1, \mathbf{x}_0, \tilde{\boldsymbol{\mu}}) = \tilde{F}^l(x_{m+1}^{l-1}|\boldsymbol{\theta}^{l,m+1}(\tau), \mathbf{x}_{1:m}^1, \mathbf{x}_0, \tilde{\boldsymbol{\mu}}) \\ &= 2 \left[\sum_{k=1}^{G_{l,m+1}} \alpha_k^{l,m+1}(\tau) \Phi_{[-1,1]}(x_{m+1}^{l-1}|\mathbf{m}_k^{l,m+1}(\tau), \sigma_k^{l,m+1}(\tau)) \right] - 1. \end{aligned} \quad (15)$$

A schematic diagram illustrating the transformation is presented in Appendix A, Figure 3.

Crucially, in (15), x_{m+1}^l depends solely on x_{m+1}^{l-1} and on $\mathbf{x}_{1:m}^1$. This implies that the Jacobian matrix of each layer of the map \mathbf{n}_{θ} has a lower triangular structure, which implies that

$$\det(\nabla_{\mathbf{x}} \mathbf{n}_{\theta(\tau)}(\mathbf{x})) = \left[\prod_{m=1}^d \frac{2}{\hat{b}_m - \hat{a}_m} \right] \prod_{l=2}^L \prod_{m=1}^d \left[2 \sum_{k=1}^{G_{l,m}} \alpha_k^{l,m} \phi_{[-1,1]}(x_m^{l-1} | \mathbf{m}_k^{l,m}, \sigma_k^{l,m}) \right]. \quad (16)$$

Using (10) and this structure of our Normalizing Flow, we look for an approximation to the TPDF that solves (3). In this approximation, the time evolution of the parameter vector $\boldsymbol{\theta}$ is determined by

(7). A key feature of the newly introduced Normalizing Flow is that, by appropriately initializing the parameters of the Gaussian mixtures, we can sharply approximate the initial condition of (3) with vanishing-variance truncated Gaussians. Moreover, a careful selection of the source distribution p_Z allows us to naturally satisfy homogeneous Dirichlet boundary conditions on $\Gamma = \partial\Omega \cap \partial\hat{\Omega}$. In fact, by ensuring that $p_Z(\mathbf{n}_\theta(\mathbf{x}))|_\Gamma = 0$, the NF will directly meet the desired boundary condition. Instead, rather than directly imposing zero-flux boundary conditions on $\partial\hat{\Omega} \setminus \Gamma$, we minimize the residual (8) and verify a posteriori that these are satisfied by the obtained numerical solution. We elaborate on these aspects in the Appendix B.

5 Bayesian Inference for Fully-Observed Diffusion Processes

We consider Bayesian inference based on a discretely observed noiseless trajectory $\mathbf{y} = [\mathbf{y}_{t_0}, \dots, \mathbf{y}_{t_n}]$ of the SDE (1), which is acquired at a constant lag Δ , to infer the parameters of the SDE $\boldsymbol{\mu}$. In this context, the posterior distribution is expressed using Bayes' rule as follows

$$\pi(\boldsymbol{\mu}|\mathbf{y}) = \frac{L(\boldsymbol{\mu}|\mathbf{y})\pi_0(\boldsymbol{\mu})}{e(\mathbf{y})}, \quad (17)$$

where L is the likelihood function, π_0 is the prior distribution, and $e(\mathbf{y}) = \int_{\Xi} L(\boldsymbol{\mu}|\mathbf{y})\pi_0(\boldsymbol{\mu})d\boldsymbol{\mu}$ is the evidence, usually not explicitly known. Thanks to the Markov property we can factorize the likelihood as follows

$$L(\boldsymbol{\mu}|\mathbf{y}) = \prod_{i=1}^n \rho(\mathbf{y}_{t_i}|t_i, t_{i-1}, \mathbf{y}_{t_{i-1}}, \boldsymbol{\mu}). \quad (18)$$

By using the approximation $\rho(\mathbf{y}_{t_i}|t_i, t_{i-1}, \mathbf{y}_{t_{i-1}}, \boldsymbol{\mu}) \simeq P(\mathbf{y}_{t_i}|\boldsymbol{\theta}(\Delta), \mathbf{y}_{t_{i-1}}, \tilde{\boldsymbol{\mu}})$, the surrogate transition density function proposed in this manuscript provides a positive estimator of the likelihood (18). Importantly, our surrogate functions as a valid probability density; thus, it can be directly utilized to conduct Bayesian inference.

Our method relies on an offline training phase during which the time-dependent parameters of the Normalizing Flow $\boldsymbol{\theta}(\tau)$ are learned by forcing P to satisfy the Fokker-Planck equation (3) for any $\tilde{\boldsymbol{\mu}} = [\boldsymbol{\mu}, s]$ of interest. Learning $\boldsymbol{\theta}(\tau)$ for $\tau \in [0, \Delta]$, rather than only at the final time $\tau = \Delta$, allows access to a time-dependent set of parameters. This enables inference even when the observations \mathbf{y} are collected asynchronously, potentially at a higher rate than Δ , thereby providing greater flexibility in real-time applications. During inference, we can amortize the computational costs incurred during training. Estimating (18) requires merely applying the change of variable formula (10) to each of the n observations $\{\mathbf{y}_{t_i}\}_{i=1}^n$, while conditioning on the previous observations $\{\mathbf{y}_{t_{j-1}}\}_{j=1}^i$ and the current state of the chain targeting (17). In the following experiments, we generate the data \mathbf{y} by simulating the SV model with an unknown parameter $\boldsymbol{\mu}^* \in \Xi$. Inference consists in sampling from the posterior distribution π given the data.

6 Numerical Results

In this section, we perform Bayesian inference for the Heston stochastic volatility model and for the SVCEV model, a non-affine extension of Heston. We assess the performance of our model in likelihood estimation by comparing it to competing methods based either on Aït-Sahalia's closed-form likelihood expansion [40], or the delta expansion of the TPDF based on the Itô-Taylor expansion proposed in [33]. An additional experiment performed in a higher-dimensional setting is included in Appendix E. The details of the data generation process, model's setup and training can be found in Appendix C, D.

6.1 Heston model

The Heston model is a two-dimensional stochastic volatility model which describes the dynamics of the log price of a stock or of the short term interest rate, whose variance is defined by the CIR process [41]. The model can be expressed as

$$\begin{cases} dV(t) = \beta(\alpha - V(t))dt + \sqrt{V(t)}\sigma dW(t) \\ dY(t) = (\mu - \frac{V(t)}{2})dt + \sqrt{V(t)}(\rho dW(t) + \sqrt{1 - \rho^2}dB(t)), \end{cases} \quad (19)$$

Table 1: Quantitative accuracy of the NF surrogate for the Heston model (19)

Metric	Value
Relative error of the log-lh (18) at μ^*	0.0003
Mean (std. error) relative $L^2(\Omega)$ error over $\{\mathbf{x}_{0,i}, \mu_i\}_{i=1}^{N_{\text{test}}}$	0.0633 (0.0123)
Relative $L^2(\Omega)$ error for $(v_0 = \epsilon, y_0, \mu^*)$	0.04 ($\epsilon = 10^{-2}$), 0.06 ($\epsilon = 10^{-4}$)

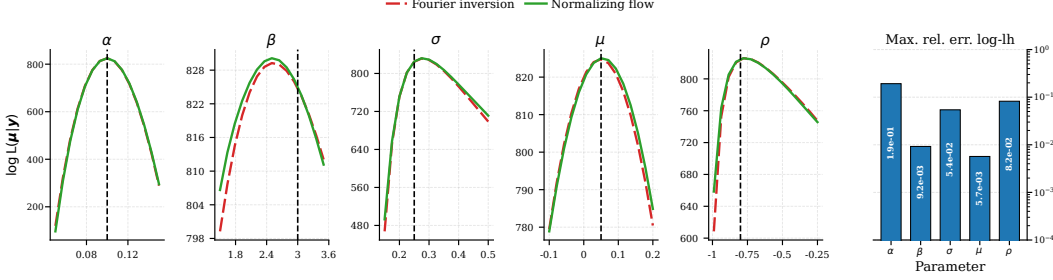


Figure 1: Log-likelihood on Heston-generated data, with error bars showing the maximum relative error for each 1D slice. Unshown parameters are fixed at μ^* ; the vertical black line marks the true parameter.

where $W(t)$ and $B(t)$ are independent Brownian motions. The Normalizing Flow is parametrized by the location of the initial condition $[V(0), Y(0)] = \mathbf{x}_0 \in \mathbb{R}^+ \times \mathbb{R}$ and by the parameters of the SDE $\mu = [\alpha, \beta, \sigma, \mu, \rho] \in \mathbb{R}^+ \times \mathbb{R}^+ \times \mathbb{R}^+ \times \mathbb{R} \times (-1, 1)$. The residual (8) is minimized over a $5 + 2 + 2$ dimensional space, which makes the problem computationally challenging for traditional solvers.

For this model, the exact characteristic function, which is the Fourier transform of the TPDF, is available in closed form [42]. We use this example to quantitatively assess the performance of our method in estimating the true likelihood, obtained via Fourier inversion of the TPDF. To accomplish this, we generate $n + 1 = 350$ synthetic observations by simulating a single trajectory of the Heston model (19), using the parameters $\mu^* = [0.1, 3, 0.25, 0.05, -0.8]$ and $\Delta = 0.5$. In Figure 1, we compare the approximation of the log-likelihood (log-lh) (18) evaluated over the observations conditioned on the true parameter μ^* . The Normalizing Flow is capable of providing an approximation that reflects the behavior of the semi-exact likelihood, making it a suitable candidate for an MCMC algorithm targeting the posterior. From a quantitative perspective, we assess the quality of the surrogate transition density in three complementary ways. First, we report the relative error between the reference log-likelihood and the NF-based log-likelihood at the true parameter μ^* . Second, we draw a batch of conditioning pairs $\{(\mathbf{x}_{0,i}, \mu_i)\}_{i=1}^{N_{\text{test}}} \sim \eta \times \hat{\pi}$ (cf. (36)), with $N_{\text{test}} = 100$. For each pair, we compute the relative $L^2(\Omega)$ error at time Δ between the reference TPDF and its NF approximation. Third, to specifically probe the challenging boundary regime of the volatility process, we report the same $L^2(\Omega)$ error on a low-volatility test case with fixed initial variance $v_0 = \epsilon$, where $\epsilon \ll 1$. The results are summarized in Table 1 and suggest that the NF generalizes properly across different parameters and is resilient in low volatility regimes.

We use the semi-exact TPDF and the surrogate model to draw samples from the posterior distribution, with MCMC. To achieve this, we use MCMC in the form of Slice Sampling with axis-aligned [43]. In Table 2, we report the empirical Wasserstein-2 (W_2) distance [44] between the reference posterior distribution and the posterior distribution drawn using NF, along with the computational runtime required to sample the chain. Importantly, our model remains comparable to Fourier transform inversion while being significantly more cost-effective and maintains high accuracy. Our approximation is much faster because it requires only n forward passes through the Flow, rather than approximating the Fourier inversion. In Appendix C.1.3, Figures 7, 8 display the marginal posterior distributions as well as the joint distribution of two out of the five parameters of the Heston model. The joint distributions for $\beta - \sigma$ and $\rho - \sigma$ show that our model effectively captures the correlation between different parameters. These results further suggest that our model is approaching the correct posterior distribution.

Table 2: Runtime for 10^4 MCMC samples, empirical joint W_2 distance between sampled posterior distributions $\pi(\boldsymbol{\mu}|\mathbf{y})$, and marginal parameter-wise W_2 distances, relative to the Fourier reference.

Model	Method	Time (s)	W_2	W_2^α	W_2^β	W_2^σ	W_2^μ	W_2^ρ
Heston (19)	Fourier	14560.13	Ref.	–	–	–	–	–
	NF	2243.37	0.066	0.0003	0.057	0.0036	0.0046	0.011

Table 3: Accuracy of the likelihood approximations for the Heston model (19). Best values in bold.

Metric	NF	A.-S.	Itô-Taylor
Relative error over the log-lh (18) given $\boldsymbol{\mu}^*$	0.0044	0.1934	0.0441
Average relative err. of log-lh over $\{\boldsymbol{\mu}^i\}_{i=1}^{N_{\text{test}}}$	0.257	4.335	3.232
Standard error (relative err. of log-lh)	0.039	0.714	0.539
Median relative err. of log-lh over $\{\boldsymbol{\mu}^i\}_{i=1}^{N_{\text{test}}}$	0.100	3.064	1.350

Finally, we generate $n + 1 = 200$ data in a low-frequency setting, using a time lag $\Delta = 1$, $\boldsymbol{\mu}^*$ as defined earlier, and compare various likelihood approximations. In Table 3, we report the relative error between the reference log-likelihood and the approximated log-likelihood at the true parameter $\boldsymbol{\mu}^*$ and averaged over a batch $\{\boldsymbol{\mu}^i\}_{i=1}^{N_{\text{test}}} \sim \hat{\pi}$ (cf. (36)) with $N_{\text{test}} = 100$. We consider both NF and the 2nd order closed-form expansion from Ait-Sahalia (A.-S.) [31] and the 4th order Itô-Taylor expansion [33]. Among the approximations evaluated, NF attains the smallest trajectory log-likelihood errors. Notably, our approach is particularly effective in the low-frequency setting and away from $\boldsymbol{\mu}^*$ because it does not rely on expansions in powers of Δ but rather a structure-preserving surrogate for the TPDF.

6.2 SVCEV

We now consider the SVCEV model, which is nonlinear, irreducible, and non-affine, and therefore its characteristic function cannot be expressed in closed-form:

$$\begin{cases} dV(t) = \beta(\alpha - V(t))dt + \sigma V^\gamma(t)dW(t) \\ dY(t) = (\mu - V(t)/2)dt + \sqrt{V(t)}(\rho dW(t) + \sqrt{1 - \rho^2}dB(t)). \end{cases} \quad (20)$$

We generate $n + 1 = 100$ data with time-lag $\Delta = 0.5$, and compare our results with a reference estimator based on data augmentation (DA) and importance sampling [45], see Appendix D for further details. In Table 4, we analyze the relative error between the reference and the approximated log-likelihood at the true parameter $\boldsymbol{\mu}^*$ and averaged over a batch $\{\boldsymbol{\mu}^i\}_{i=1}^{N_{\text{test}}} \sim \hat{\pi}$ (cf. (41)) with $N_{\text{test}} = 100$. We compare our method (NF), the 2nd order closed-form approximation of A.-S. [31], and the 4th order Itô-Taylor expansion [33]. From this table, we can conclude that the true error is upper-bounded by the sum of the discrepancy with respect to the DA reference and the DA estimator’s error. NF yields the smallest discrepancies, even away from $\boldsymbol{\mu}^*$, underscoring the benefit of learning the TPDF over $\hat{\pi}$ for Bayesian inference. By contrast, we observed that closed-form transition-density expansions can become unstable and, in some cases, diverge when evaluated far from $\boldsymbol{\mu}^*$.

Lastly, in Figure 2, we evaluate the quality of the log-likelihood and posterior distribution obtained by the Normalizing Flow against the data augmentation reference. The results show good agreement, indicating that the surrogate Normalizing Flow extends its applicability beyond the affine Heston framework. Additionally, as shown in Table 5, we find that the Normalizing Flow yields a substantial computational speed-up, making it a more efficient alternative to traditional inference methodologies.

Table 4: Relative log-likelihood discrepancies for the SVCEV model (20). Best values in bold. At μ^* , the DA estimator itself has estimated relative error 5.5×10^{-4} with 95% CI $[4.96, 5.96] \times 10^{-4}$.

Metric	NF	A.-S.	Itô-Taylor
Relative err. of the log-lh (18) at μ^*	0.0004	0.0063	0.0091
Average relative err. of log-lh over $\{\mu^i\}_{i=1}^{N_{\text{test}}}$	0.084	0.941	0.811
Standard error (relative err. of log-lh)	0.014	0.163	0.112

Table 5: SVCEV model (20): runtime for 10^4 MCMC samples and empirical W_2 distance relative to the DA reference. A.-S. is omitted as it does not target the posterior.

Metric	Data augmentation	Normalizing Flow	Itô Taylor
Time (s)	63541.69	1389.25	7219.16
W_2 distance	Reference	0.412	1.337

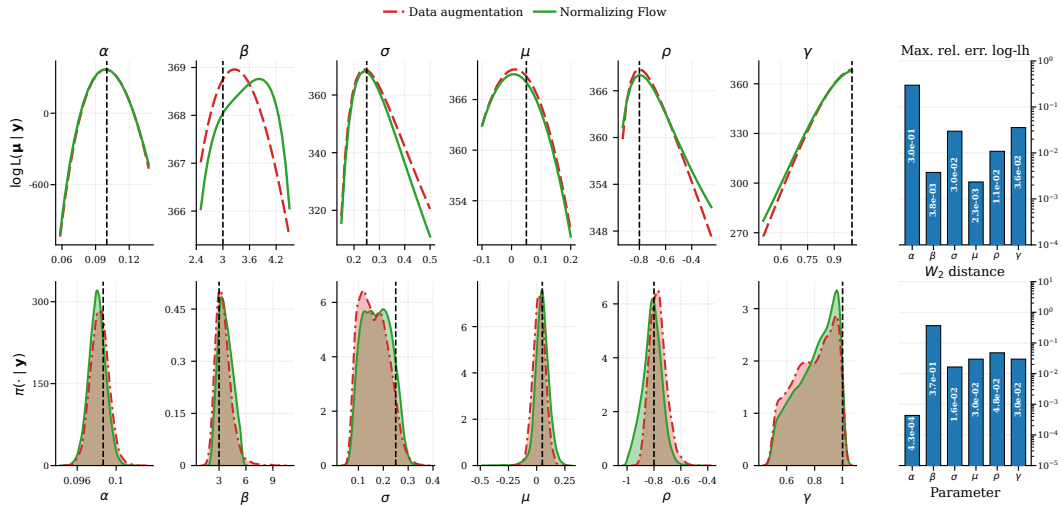


Figure 2: Top: log-lh slices for SVCEV data, with bars of the maximum relative-error of log-lh and all other parameters fixed at μ^* . Bottom: posterior marginals with corresponding W_2 distances.

7 Future directions and limitations

In this work, we have proposed a surrogate model based on Neural Galerkin and Normalizing Flows for likelihood estimation and Bayesian inference of diffusion processes. Compared with traditional inference techniques, NFs offer significant accuracy and computational advantages, revealing a powerful tool for exploring high-dimensional posterior distributions of SDE parameters. We focused on fully observed processes; nevertheless, our model can be combined with particle-based MCMC methods to infer partially observed diffusions, a direction we leave for future research.

A key assumption of our work is that the target density can be effectively modeled using a distribution with compact support. The model's accuracy is not guaranteed in the tails of the distributions, which makes it unsuitable for directly simulating extreme events. Likewise, the reference distribution of the NF may not accurately represent the tail decay in the inaccessible boundary. A possible remedy is to parameterize and train this reference density, which we will explore in future research. In this extension, our approach would be well-suited for modeling processes living in bounded domains, such as those associated with Fisher-Wright type SDEs with inaccessible boundaries. Finally, future research will explore our methodology and the generative potential of Normalizing Flows as a promising route for modeling and inference of McKean-Vlasov SDEs.

References

- [1] Alexandros Beskos, Omiros Papaspiliopoulos, Gareth O. Roberts, and Paul Fearnhead. Exact and Computationally Efficient Likelihood-Based Estimation for Discretely Observed Diffusion Processes (with Discussion). *Journal of the Royal Statistical Society: Series B (Statistical Methodology)*, 68(3):333–382, 2006.
- [2] Giorgos Sermaidis, Omiros Papaspiliopoulos, Gareth O. Roberts, Alexandros Beskos, and Paul Fearnhead. Markov Chain Monte Carlo for Exact Inference for Diffusions. *Scandinavian Journal of Statistics*, 40(2):294–321, 2013.
- [3] Bjorn Eraker. MCMC Analysis of Diffusion Models with Application to Finance. *Journal of Business & Economic Statistics*, 19(2):177–191, 2001.
- [4] Omar Elerian, Siddhartha Chib, and Neil Shephard. Likelihood Inference for Discretely Observed Nonlinear Diffusions. *Econometrica*, 69(4):959–993, 2001.
- [5] Christophe Andrieu and Gareth O. Roberts. The Pseudo-Marginal Approach for Efficient Monte Carlo Computations. *The Annals of Statistics*, 37(2):697–725, 2009.
- [6] Christophe Andrieu, Arnaud Doucet, and Roman Holenstein. Particle Markov chain Monte Carlo methods. *Journal of the Royal Statistical Society: Series B (Statistical Methodology)*, 72(3):269–342, 2010.
- [7] Christiane Fuchs. Bayesian Inference for Diffusions with Low-Frequency Observations. In *Inference for Diffusion Processes: With Applications in Life Sciences*, pages 171–278. Springer, 2013.
- [8] Gareth O. Roberts and Osnat Stramer. On Inference for Non-linear Diffusion Models Using Metropolis-Hastings Algorithms. *Biometrika*, 88(3):603–621, 2001.
- [9] Iosif Ilyich Gikhman and Anatoli Vladimirovich Skorokhod. *Stochastic Differential Equations*. Springer-Verlag, New York, Heidelberg, 1972.
- [10] Maziar Raissi, Paris Perdikaris, and George Em Karniadakis. Physics-informed neural networks: A deep learning framework for solving forward and inverse problems involving nonlinear partial differential equations. *Journal of Computational Physics*, 378:686–707, 2019.
- [11] Justin Sirignano and Konstantinos Spiliopoulos. DGM: A deep learning algorithm for solving partial differential equations. *Journal of Computational Physics*, 375:1339–1364, 2018.
- [12] Jiequn Han, Arnulf Jentzen, and Weinan E. Solving high-dimensional partial differential equations using deep learning. *Proceedings of the National Academy of Sciences*, 115(34):8505–8510, 2018.
- [13] George Em Karniadakis, Ioannis G. Kevrekidis, Lu Lu, Paris Perdikaris, Sifan Wang, and Liu Yang. Physics-informed machine learning. *Nature Reviews Physics*, 3(6):422–440, 2021.
- [14] Alfio Quarteroni, Paola Gervasio, and Francesco Regazzoni. Combining physics-based and data-driven models: advancing the frontiers of research with scientific machine learning. *Mathematical Models and Methods in Applied Sciences*, page 1–167, March 2025.
- [15] Haozhe Su, M. V. Tretyakov, and David P. Newton. Deep Learning of Transition Probability Densities for Stochastic Asset Models with Applications in Option Pricing. *Management Science*, 70(7):4428–4449, 2024.
- [16] Yubin Lu, Romit Maulik, Ting Gao, Felix Dietrich, Ioannis G Kevrekidis, and Jinqiao Duan. Learning the temporal evolution of multivariate densities via normalizing flows. *Chaos: An Interdisciplinary Journal of Nonlinear Science*, 32(3), 2022.
- [17] Kejun Tang, Xiaoliang Wan, and Qifeng Liao. Adaptive deep density approximation for Fokker-Planck equations. *Journal of Computational Physics*, 457:111080, 2022.

- [18] Xiaodong Feng, Tao Zhou, and Li Zeng. Solving Time Dependent Fokker-Planck Equations via Temporal Normalizing Flow. *Communications in Computational Physics*, 32(2):401–423, January 2022.
- [19] Aditi Krishnapriyan, Amir Gholami, Shandian Zhe, Robert Kirby, and Michael W Mahoney. Characterizing possible failure modes in physics-informed neural networks. *Advances in neural information processing systems*, 34:26548–26560, 2021.
- [20] Arka Daw, Jie Bu, Sifan Wang, Paris Perdikaris, and Anuj Karpatne. Mitigating Propagation Failures in Physics-informed Neural Networks using Retain-Resample-Release (R3) Sampling. In Andreas Krause, Emma Brunskill, Kyunghyun Cho, Barbara Engelhardt, Sivan Sabato, and Jonathan Scarlett, editors, *Proceedings of the 40th International Conference on Machine Learning*, volume 202 of *Proceedings of Machine Learning Research*, pages 7264–7302. PMLR, 23–29 Jul 2023.
- [21] Riccardo Saporiti and Fabio Nobile. Neural Galerkin Normalizing Flow for Transition Probability Density Functions of Diffusion Models. *arXiv preprint arXiv:2603.18907*, 2026.
- [22] Joan Bruna, Benjamin Peherstorfer, and Eric Vanden-Eijnden. Neural Galerkin schemes with active learning for high-dimensional evolution equations. *Journal of Computational Physics*, 496:112588, 2024.
- [23] Matthew M. Graham, Alexandre H. Thiery, and Alexandros Beskos. Manifold Markov Chain Monte Carlo Methods for Bayesian Inference in Diffusion Models. *Journal of the Royal Statistical Society Series B: Statistical Methodology*, 84(4):1229–1256, 04 2022.
- [24] Andrew Golightly and Chris Sherlock. Augmented pseudo-marginal Metropolis–Hastings for partially observed diffusion processes. *Statistics and Computing*, 32(1):21, Feb 2022.
- [25] Ajay Jasra, Kengo Kamatani, and Amin Wu. Bayesian inference for non-synchronously observed diffusions. *SIAM/ASA Journal on Uncertainty Quantification*, 14(2):369–393, 2026.
- [26] Jaromir Sant, Paul A Jenkins, Jere Koskela, and Dario Spano. Bayesian inference from time series of allele frequency data using exact simulation techniques. *arXiv preprint arXiv:2502.12279*, 2025.
- [27] Celia García-Pareja and Fabio Nobile. Unbiased Likelihood Estimation of Wright–Fisher Diffusion Processes. In *International Conference on Monte Carlo and Quasi-Monte Carlo Methods in Scientific Computing*, pages 259–275. Springer, 2022.
- [28] Umberto Picchini. Inference for SDE Models via Approximate Bayesian Computation. *Journal of Computational and Graphical Statistics*, 23(4):1080–1100, 2014.
- [29] Petar Jovanovski, Andrew Golightly, and Umberto Picchini. Towards Data-Conditional Simulation for ABC Inference in Stochastic Differential Equations. *Bayesian Analysis*, 21(1):309 – 339, 2026.
- [30] Tom Ryder, Andrew Golightly, A Stephen McGough, and Dennis Prangle. Black-box variational inference for stochastic differential equations. In *International Conference on Machine Learning*, pages 4423–4432. PMLR, 2018.
- [31] Yacine Aït-Sahalia. Closed-form likelihood expansions for multivariate diffusions. *The Annals of Statistics*, 36(2):906–937, 2008.
- [32] Seungmoon Choi. Explicit form of approximate transition probability density functions of diffusion processes. *Journal of Econometrics*, 187(1):57–73, 2015.
- [33] Nian Yang, Nan Chen, and Xiangwei Wan. A new delta expansion for multivariate diffusions via the Itô-Taylor expansion. *Journal of Econometrics*, 209(2):256–288, 2019.
- [34] Yuga Iguchi and Alexandros Beskos. A closed-form transition density expansion for elliptic and hypo-elliptic SDEs. *arXiv preprint arXiv:2502.07047*, 2025.
- [35] Grigorios A. Pavliotis. *Stochastic Processes and Applications*. Springer New York, NY, 2014.

- [36] Vladimir Lucic. Boundary conditions for computing densities in hybrid models via PDE methods. *Stochastics*, 84(5-6):705–718, 2012.
- [37] Bernd Engelmann, Frank Koster, and Daniel Oeltz. Calibration of the Heston stochastic local volatility model: A finite volume scheme. *International Journal of Financial Engineering*, 08(01):2050048, 2021.
- [38] David Chin-Lung Fong and Michael Saunders. LSMR: An Iterative Algorithm for Sparse Least-Squares Problems. *SIAM Journal on Scientific Computing*, 33(5):2950–2971, 2011.
- [39] Norman L. Johnson, Samuel Kotz, and Narayanaswamy Balakrishnan. *Continuous Univariate Distributions, Volume 2*. John Wiley & Sons, 1995.
- [40] Yacine Aït-Sahalia and Robert Kimmel. Maximum likelihood estimation of stochastic volatility models. *Journal of Financial Economics*, 83(2):413–452, 2007.
- [41] John C. Cox, Jonathan E. Ingersoll, and Stephen A. Ross. A Theory of the Term Structure of Interest Rates. *Econometrica*, 53(2):385–407, 1985.
- [42] C. Lamoureux and A. Paseka. Information in Option Prices and the Underlying Asset Dynamics. *Working paper, Eller School of Business, University of Arizona*, 2005.
- [43] Radford M. Neal. Slice sampling. *The Annals of Statistics*, 31(3):705–767, 2003.
- [44] Cédric Villani. *Optimal Transport: Old and New*, volume 338 of *Grundlehren der Mathematischen Wissenschaften*. Springer, Berlin, Heidelberg, 2009.
- [45] Garland B Durham and A. Ronald Gallant. Numerical Techniques for Maximum Likelihood Estimation of Continuous-Time Diffusion Processes. *Journal of Business & Economic Statistics*, 20(3):297–338, 2002.
- [46] Osnat Stramer and Matthew Bognar. Bayesian Inference for Irreducible Diffusion Processes Using the Pseudo-Marginal Approach. *Bayesian Analysis*, 6(2):231–258, 2011.
- [47] Ilya I. Gikhman. A Short Remark on Feller’s Square Root Condition. SSRN Working Paper, 2011.
- [48] Adam Paszke, Sam Gross, Francisco Massa, Adam Lerer, James Bradbury, Gregory Chanan, Trevor Killeen, Zeming Lin, Natalia Gimelshein, Luca Antiga, et al. Pytorch: An imperative style, high-performance deep learning library. *Advances in neural information processing systems*, 32, 2019.
- [49] George Papamakarios, David Sterratt, and Iain Murray. Sequential Neural Likelihood: Fast Likelihood-free Inference with Autoregressive Flows. In Kamalika Chaudhuri and Masashi Sugiyama, editors, *Proceedings of the Twenty-Second International Conference on Artificial Intelligence and Statistics*, volume 89 of *Proceedings of Machine Learning Research*, pages 837–848. PMLR, 16–18 Apr 2019.
- [50] Pierluigi Balduzzi, Sanjiv R. Das, Silverio Foresi, and Rangarajan K. Sundaram. A Simple Approach to Three-Factor Affine Term Structure Models. *Journal of Fixed Income*, 6(1):43–53, 1996.
- [51] H. E. Daniels. Saddlepoint Approximations in Statistics. *The Annals of Mathematical Statistics*, 25(4):631–650, 1954.
- [52] Yaniv Leviathan, Matan Kalman, and Yossi Matias. Fast inference from transformers via speculative decoding. In *International Conference on Machine Learning*, pages 19274–19286. PMLR, 2023.

A Structure of the Normalizing Flow

The multi-layer schematic of the bounded Normalizing Flow is shown in Figure 3.

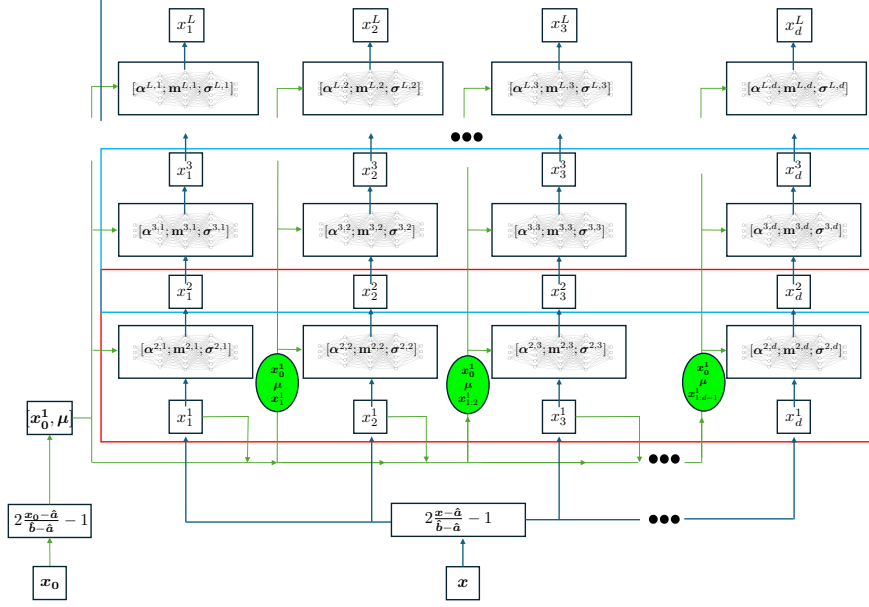


Figure 3: Transformation executed by the Normalizing Flow (11) across layers $l = 1, \dots, L$. Moving from bottom to top, each column $m = 1, \dots, d$ transforms x_m while conditioning on $x_{1:m-1}^1, x_0, \mu$.

B Approximation of the Dirac delta and zero-flux boundary conditions

B.1 Imposition of the Dirac delta initial condition

The bounded Normalizing Flow enables us to utilize the Jacobian of the determinant from the transformation (16) for representing the initial condition of the Fokker-Planck PDE. To do this, we initialize weights and biases of the output layer of the d Neural Networks of the second set of bijection $n_{\theta^2(\tau)}^{2,m+1}$, for $m = 0, \dots, d-1$, to zero. Specifically, only the entries of $\theta^2(0)$ that compose the weights and biases of the last layer of the Neural Network are initialized to zero. The variances of the Gaussian distributions in the mixture of this layer are set to an arbitrary tolerance $\hat{\epsilon} > 0$, which approaches zero. Simultaneously, we adjust the means of these Gaussian distributions to coincide with the location of the initial condition, x_0 . The weights of the Gaussians are initialized uniformly. This initialization results in mixtures of truncated Gaussians with the following parameters

$$\begin{cases} m_k^{2,m+1} = x_{0,m+1}, & \text{for } m = 0, \dots, d-1, k = 1, \dots, G_{2,m+1}, \\ \sigma_k^{2,m+1} = \hat{\epsilon} & \text{for } m = 0, \dots, d-1, k = 1, \dots, G_{2,m+1}, \\ \alpha_k^{2,m+1} = 1/G_{2,m+1} & \text{for } m = 0, \dots, d-1, k = 1, \dots, G_{2,m+1}. \end{cases} \quad (21)$$

As a result, the transformation collapses to a step function, contributing to the determinant as " $\frac{\partial n_{\theta^1(\tau)}^{2,m}(x_m^1)}{\partial x_m^1} \simeq \delta_{x_0}((x^0)_m)$ " for $m = 1, \dots, d$. These transformations map all the elements satisfying the componentwise inequality $x \geq x_0$ to $\mathbf{1}$ and the remaining elements to $-\mathbf{1}$. The weights of the Neural Networks in the subsequent layers of the Flow are initialized randomly, and positive variance is ensured by applying the softplus activation function. Consequently, compared to the contribution from the determinant of the Jacobian of the transformation in the second layer, the contributions to $\det(\nabla_x n_\theta)$ from the following layers (for $l \geq 3$) are negligible. The resulting density is not

Table 6: A posteriori verification of the zero-flux boundary condition on $\partial\hat{\Omega} \setminus \Gamma$ over $N_{\text{test}} = 100$ test pairs $\{(\mathbf{x}_{0,i}, \boldsymbol{\mu}_i)\}_{i=1}^{N_{\text{test}}} \sim \eta \times \tilde{\pi}_0$.

Model	Quantity	Mean	Std. dev.	95% CI for mean
Heston	Time-integrated flux (24)	3.08×10^{-11}	7.71×10^{-11}	$[2.01, 4.15] \times 10^{-11}$
	Maximum absolute flux (25)	2.34×10^{-8}	1.36×10^{-7}	$[3.97, 5.52] \times 10^{-8}$
SVCEV	Time-integrated flux (24)	5.87×10^{-10}	3.05×10^{-9}	$[1.64, 10.09] \times 10^{-10}$
	Maximum absolute flux (25)	2.40×10^{-7}	1.43×10^{-6}	$[2.54, 56.29] \times 10^{-8}$

negligible only in a neighborhood of \mathbf{x}_0 , and its sharpness is calibrated heuristically and controlled by $\hat{\epsilon}$.

We further remark that the strength of the Flow’s structure based on Gaussian mixture models lies in its ability to approximate the Dirac delta distribution with only the first trainable layer.

B.2 Zero-flux boundary conditions

When we truncate the domain Ω into $\hat{\Omega}$, we theoretically impose zero-flux boundary conditions on $\partial\hat{\Omega} \setminus \Gamma$. For the diffusion process (1), these conditions are expressed as follows:

$$\mathbf{J}(\mathbf{x}, t, s, \mathbf{x}_0, \boldsymbol{\mu}) \cdot \mathbf{n} = 0 \quad \text{for all } \mathbf{x} \in \partial\hat{\Omega} \setminus \Gamma, \quad (22)$$

where \mathbf{n} is the outer normal unit vector at $\partial\hat{\Omega} \setminus \Gamma$ and

$$\mathbf{J}(\mathbf{x}, t, s, \mathbf{x}_0, \boldsymbol{\mu}) = \mathbf{b}(t, \mathbf{x}, \boldsymbol{\mu})\rho(\mathbf{x}|t, s, \mathbf{x}_0, \boldsymbol{\mu}) - \frac{1}{2}\nabla_{\mathbf{x}} \cdot (\Sigma(t, \mathbf{x}, \boldsymbol{\mu})\rho(\mathbf{x}|t, s, \mathbf{x}_0, \boldsymbol{\mu})). \quad (23)$$

In our experiments, instead of imposing the boundary condition given in (22), we verify that these conditions are satisfied by the numerical solution. This approach is justified by the expectation that, since we initialize the dynamics from a Dirac distribution, most of the mass of the TPDF will be contained within $\hat{\Omega}$, provided that $\hat{\Omega}$ is sufficiently large. To support our statement, we verify that our solution satisfies

$$\int_s^{s+\Delta} \int_{\partial\hat{\Omega} \setminus \Gamma} |\mathbf{J}(\mathbf{x}, t, s, \mathbf{x}_0, \boldsymbol{\mu}) \cdot \mathbf{n}| d\mathbf{x} dt \simeq 0. \quad (24)$$

We validate this observation for both the Heston model (19) and the SVCEV model (20). For each model, we sample $N_{\text{test}} = 100$ conditioning pairs $\{(\mathbf{x}_{0,i}, \boldsymbol{\mu}_i)\}_{i=1}^{N_{\text{test}}} \sim \eta \times \tilde{\pi}_0$. For each pair, we use our Normalizing Flow to approximate (22) and apply the trapezoidal rule to integrate (24) in both time and space. Table 6 reports the empirical mean, standard deviation, and 95% confidence interval of the numerical approximation of (24) and of the maximum absolute flux

$$\max_{(t, \mathbf{x}) \in [s, s+\Delta] \times \partial\hat{\Omega} \setminus \Gamma} |\mathbf{J}(\mathbf{x}, t, s, \mathbf{x}_0, \boldsymbol{\mu}) \cdot \mathbf{n}|. \quad (25)$$

B.2.1 Imposition of the zero-flux boundary conditions in the Neural Galerkin framework

As an alternative, we propose an approach to impose zero-flux boundary conditions while integrating the dynamics (7). Rather than minimizing (8) alone, one could tackle the minimization problem

$$\begin{aligned} \min_{\boldsymbol{\zeta} \in \hat{\Theta}} & \int_{\Xi^*} \int_{\Omega} \int_{\Omega} |r_{s+\tau, s}(\boldsymbol{\theta}, \boldsymbol{\zeta}, \mathbf{x}, \mathbf{x}_0, \tilde{\boldsymbol{\mu}})|^2 d\nu_{\theta(\tau)}(\mathbf{x}|\mathbf{x}_0, \tilde{\boldsymbol{\mu}}) d\eta(\mathbf{x}_0) d\tilde{\pi}_0^*(\tilde{\boldsymbol{\mu}}) \\ & + \epsilon \int_{\Xi^*} \int_{\Omega} \int_{\partial\hat{\Omega} \setminus \Gamma} |\nabla_{\boldsymbol{\theta}} \mathbf{P}(\mathbf{x}|\boldsymbol{\theta}(\tau), \mathbf{x}_0, \tilde{\boldsymbol{\mu}})\boldsymbol{\zeta} - \frac{1}{\epsilon}\varphi(\mathbf{x}, t, s, \mathbf{x}_0, \boldsymbol{\mu})|^2 d\tilde{\nu}(\mathbf{x}|\mathbf{x}_0, \tilde{\boldsymbol{\mu}}) d\eta(\mathbf{x}_0) d\tilde{\pi}_0^*(\tilde{\boldsymbol{\mu}}), \end{aligned} \quad (26)$$

where $\epsilon > 0$ is a regularization parameter and $\tilde{\nu}$ is a positive measure over $\partial\hat{\Omega} \setminus \Gamma$. The minimizers of (26) are given by the Euler-Lagrange equations

$$(M^i(\boldsymbol{\theta}) + \epsilon M^b(\boldsymbol{\theta}))\boldsymbol{\zeta} = \mathbf{F}^i(t, \boldsymbol{\theta}) + \mathbf{F}^b(t, \boldsymbol{\theta}), \quad (27)$$

where the internal contributions read

$$\begin{aligned}
M^i(\boldsymbol{\theta}) &= \int_{\Xi^*} \int_{\Omega} \int_{\Omega} \nabla_{\boldsymbol{\theta}} P(\mathbf{x}|\boldsymbol{\theta}(\tau), \mathbf{x}_0, \tilde{\boldsymbol{\mu}}) \nabla_{\boldsymbol{\theta}} P(\mathbf{x}|\boldsymbol{\theta}(\tau), \mathbf{x}_0, \tilde{\boldsymbol{\mu}})^T d\nu_{\boldsymbol{\theta}(\tau)} d\eta d\tilde{\pi}_0^*, \\
\mathbf{F}^i(t, \boldsymbol{\theta}) &= \int_{\Xi^*} \int_{\Omega} \int_{\Omega} \nabla_{\boldsymbol{\theta}} P(\mathbf{x}|\boldsymbol{\theta}(\tau), \mathbf{x}_0, \tilde{\boldsymbol{\mu}}) \mathcal{L}_t^*(P(\cdot|\boldsymbol{\theta}(\tau), \mathbf{x}_0, \tilde{\boldsymbol{\mu}}))(\mathbf{x}) d\nu_{\boldsymbol{\theta}(\tau)} d\eta d\tilde{\pi}_0^*,
\end{aligned} \tag{28}$$

while the boundary contributions are given by

$$\begin{aligned}
M^b(\boldsymbol{\theta}) &= \int_{\Xi^*} \int_{\Omega} \int_{\partial\hat{\Omega}\setminus\Gamma} \nabla_{\boldsymbol{\theta}} P(\mathbf{x}|\boldsymbol{\theta}(\tau), \mathbf{x}_0, \tilde{\boldsymbol{\mu}}) \nabla_{\boldsymbol{\theta}} P(\mathbf{x}|\boldsymbol{\theta}(\tau), \mathbf{x}_0, \tilde{\boldsymbol{\mu}})^T d\tilde{\nu} d\eta d\tilde{\pi}_0^*, \\
\mathbf{F}^b(t, \boldsymbol{\theta}) &= \int_{\Xi^*} \int_{\Omega} \int_{\partial\hat{\Omega}\setminus\Gamma} \nabla_{\boldsymbol{\theta}} P(\mathbf{x}|\boldsymbol{\theta}(\tau), \mathbf{x}_0, \tilde{\boldsymbol{\mu}}) \varphi(\mathbf{x}, t, s, \mathbf{x}_0, \boldsymbol{\mu}) d\tilde{\nu} d\eta d\tilde{\pi}_0^*.
\end{aligned} \tag{29}$$

It can be shown that, as $\epsilon \rightarrow 0$, (27) coincides with the weak formulation of the Fokker-Planck equation (3) on the bounded domain $\hat{\Omega}$ with zero-flux boundary conditions on $\partial\hat{\Omega} \setminus \Gamma$ and homogeneous Dirichlet data on Γ , taking as test function $\nabla_{\boldsymbol{\theta}} P$. We plan to explore this alternative approach for imposing zero-flux boundary conditions in future studies.

C Setup and further validation for the Heston Stochastic Volatility Model

To generate the data for the test case, we use the Euler-Maruyama scheme to simulate a trajectory of $n + 1 = 350$ observations with parameter values of $\alpha^* = 0.1$, $\beta^* = 3$, $\sigma^* = 0.25$, $\mu^* = 0.05$, and $\rho^* = -0.8$. The observation gap is set to $\Delta = 0.5$. To minimize discretization errors, as outlined in references [40, 46], we introduce a discretization made of 100 sub-intervals per sampling interval. We generate a total of 700 observations and then drop the first 350. These last 350 observations constitute our data $\mathbf{y} = [\mathbf{y}_{t_0}, \dots, \mathbf{y}_{t_{349}}]$.

As the SDE in equation (19) is autonomous, we can set the initial time for integration to an arbitrary value, such as $s = 0$. Thus, the dynamics can be integrated from that time onward. Let $\mathbf{x} = [v, y]$ and let us denote $\rho(\mathbf{x}|t) = \rho(\mathbf{x}|t, 0, \mathbf{x}_0, \boldsymbol{\mu})$. The Fokker-Planck equation associated with (19) reads

$$\begin{cases} \begin{aligned} &\partial_t \rho(\mathbf{x}|t) + (\mu - v/2) \partial_y \rho(\mathbf{x}|t) + \beta(\alpha - v) \partial_v \rho(\mathbf{x}|t) \\ &- \beta \rho(\mathbf{x}|t) \\ &- \frac{1}{2} (v \partial_y^2 \rho(\mathbf{x}|t) + \sigma^2 v \partial_v^2 \rho(\mathbf{x}|t) + 2\rho \sigma v \partial_{yv}^2 \rho(\mathbf{x}|t)) \\ &- \rho \sigma \partial_y \rho(\mathbf{x}|t) - \sigma^2 \partial_v \rho(\mathbf{x}|t) = 0 \end{aligned} & (v, y) \in \mathbb{R}^+ \times \mathbb{R}, t \in (0, T], \\ \rho(v = 0, y|t, 0, \mathbf{x}_0, \boldsymbol{\mu}) = 0 & \text{for } y \in \mathbb{R}, t \in (0, T], \\ \rho(\mathbf{x}|0, 0, \mathbf{x}_0, \boldsymbol{\mu}) = \delta_{\mathbf{x}_0}(\mathbf{x}) & \text{for } (v, y) \in \mathbb{R}^+ \times \mathbb{R}, t \in \{0\}. \end{cases} \tag{30}$$

We adhere to the strict Feller condition [47] regarding the SDE parameters, specifically $\sigma < \sqrt{2\alpha\beta}$. This condition justifies the boundary condition $\rho(0, y|t, 0, \mathbf{x}_0, \boldsymbol{\mu}) = 0$.

C.1 Structure of the Normalizing Flow

The TPDF of (19) can be decomposed as

$$p_{V,Y}(v, y|v_0, y_0) = p_V(v|v_0, y_0) p_{Y|V}(y|v, y_0, v_0). \tag{31}$$

This decomposition (31) guides the construction of the transport map of the Flow $\mathbf{n}_{\theta}(v, y)$, which is defined by conditioning. The first component of $\mathbf{n}_{\theta}(v, y)$ updates the volatility variable, while the second component modifies the asset price conditioned on the volatility.

We solve the equation (30) in the bounded domain $\hat{\Omega} = (0, 3) \times (-6.5, 6.5)$, therefore, we set $\hat{\mathbf{a}} = [0, -6.5]$ and $\hat{\mathbf{b}} = [3, 6.5]$. The reference distribution of the Normalizing Flow is defined as the product of a Gamma distribution, truncated over the domain $[0, 1]$, for the first component of the transport map (corresponding to the volatility), and a uniform distribution over $[0, 1]$ for the second component (corresponding to the asset price). The shape parameter of the Gamma distribution is

Algorithm 1 Integration of the Neural Galerkin dynamics of the parameters of the Normalizing Flow (7).

INPUT: Normalizing Flow n_θ , reference distribution Z , prior over SDE parameters $\tilde{\pi}_0^*$, density for the location of the initial condition $\eta(\mathbf{x}_0)$, integration time-horizon Δ

OUTPUT: Set of parameters $\{\boldsymbol{\theta}(\tau)\}_{\tau \in I}$

```

1:  $\boldsymbol{\theta}(0)$  ▷ Initialize weights and biases of the NF (cf. section B).
2:  $\tau = 0$ 
3: while  $\tau < \Delta$  do
4:    $\{\mathbf{x}_{0,i}\}_{i=1}^N \sim \eta$  ▷ Draw a batch of locations of the Dirac delta initial conditions.
5:    $\{\boldsymbol{\mu}_i\}_{i=1}^N \sim \tilde{\pi}_0^*$  ▷ Draw a batch of parameters.
6:    $\{\mathbf{x}_i\}_{i=1}^N \sim \{P(\cdot | \boldsymbol{\theta}(\tau), \mathbf{x}_{0,i}, \boldsymbol{\mu}_i)\}_{i=1}^N$  ▷ Use Algorithm 2 to sample from the NF.
7:    $\mathbf{f}_{\tau,i} = \mathcal{L}_{s_i+\tau}^*(P(\cdot | \boldsymbol{\theta}(\tau), \mathbf{x}_{0,i}, \boldsymbol{\mu}_i))(\mathbf{x}_i)$ 
8:    $(J)_{ik} = \frac{\partial P(\mathbf{x}_i | \boldsymbol{\theta}(\tau), \mathbf{x}_{0,i}, \boldsymbol{\mu}_i)}{\partial \theta_k}$ 
9:    $\dot{\boldsymbol{\theta}}(\tau) \in \arg \min_{\zeta \in \dot{\Theta}} J_\tau(\boldsymbol{\theta}(\tau), \zeta)$  ▷ Using LSMR, solve (8).
10:  Update  $\boldsymbol{\theta}(\tau)$  from  $\dot{\boldsymbol{\theta}}(\tau)$  according to the RK5(4) integrator.
11:  Update  $\tau$  according to the RK5(4) integrator.
12: end while

```

set to 5/2, and its scale parameter is set to 1/2. To work with reference distributions supported in the interval $[0, 1]$, a linear scaling is applied after the last transformation 15. This scaling has the following expression

$$f(\mathbf{x}) = \frac{\mathbf{x} + 1}{2} \quad (32)$$

and maps $[-1, 1]^d$ to $[0, 1]^d$. The truncated Gamma distribution allows us to impose the boundary condition in equation (30). Similar observations apply to the other numerical experiments conducted. We use $L = 4 + 1$ layers for the Normalizing Flow. The number of elements in each MTG is set to 7. The network contains two GRU layers, each with hidden size 8. This results in a parameter vector $\boldsymbol{\theta}(\tau) \in \mathbb{R}^M$, with $M = 8448$. To approximate the Neural Galerkin residual (8), we choose $\eta(\mathbf{x}_0)$ as

$$\eta(\mathbf{x}_0) = \mathcal{U}(v_0; [0, 0.25])\mathcal{U}(y_0; [-3.5, 2.5]). \quad (33)$$

We utilize a flat prior restricted to the parameters' domain for the Bayesian inference, namely

$$\pi_0(\boldsymbol{\mu}) = 1_{\{\alpha > 0\}} 1_{\{\beta > 0\}} 1_{\{\sigma \in (0, \sqrt{2\alpha\beta})\}} 1_{\{-1 < \rho < 1\}} 1_{\{\mu \in \mathbb{R}\}}. \quad (34)$$

Notice that this distribution guarantees that the Feller condition is always satisfied.

We train the model by sampling the parameters $\boldsymbol{\mu}$ from the following distribution

$$\tilde{\pi}_0(\boldsymbol{\mu}) = 1_{\{\alpha > 0\}} \phi(\alpha | 0.1, 0.08) 1_{\{\beta > 0\}} \phi(\beta | 3, 0.2) \times \\ 1_{\{\sigma \in (0, \sqrt{2\alpha\beta})\}} \phi(\sigma | 0.25, 0.08) \phi(\mu | 0.05, 0.03) 1_{\{-1 \leq \rho \leq 1\}} \phi(\rho | -0.8, 0.08). \quad (35)$$

We employ a Monte-Carlo estimator based on 15000 samples. The dynamics satisfied by $\dot{\boldsymbol{\theta}}(\tau)$ (7), is integrated using an Explicit Runge-Kutta (RK) method of order 5(4), see Algorithm 1. The offline time required to integrate this dynamics (training time) was approximately 48h.¹

In Tables 1, 8, we test the model on the distribution

$$\hat{\pi}(\boldsymbol{\mu}) = 1_{\{\alpha > 0\}} \phi(\alpha | 0.075, 0.1) 1_{\{\beta > 0\}} \phi(\beta | 3, 0.2) \times \\ 1_{\{\sigma \in (0, \sqrt{2\alpha\beta})\}} \phi(\sigma | 0.25, 0.1) \phi(\mu | 0.05, 0.1) 1_{\{-1 \leq \rho \leq 1\}} \phi(\rho | -0.8, 0.1). \quad (36)$$

In the numerical experiments, we run an MCMC chain of length 13000 and discard the first 3000 samples as burn-in. For the implementation of MCMC in the form of slice sampling, we rely on the code released in [49]. The computational setup is summarized in Table 7.

¹All experiments were implemented in PyTorch [48] and run on a GPU cluster equipped with NVIDIA H100 SXM5 GPUs (4 GPUs per node, 94 GB GPU memory per GPU).

Quantity	Symbol	Value
Diffusion domain	Ω	$\mathbb{R}^+ \times \mathbb{R}$
Parameter of the support of the NF (Volatility)	$[\hat{a}_1, \hat{b}_1]$	[0,3]
Parameter of the support of the NF (log-Asset)	$[\hat{a}_2, \hat{b}_2]$	[-6.5,6.5]
Initial condition distribution	$\eta(v_0, y_0)$	See (33)
Parameter training distribution	$\tilde{\pi}_0(\boldsymbol{\mu})$	See (35)
Parameter test distribution	$\hat{\pi}(\boldsymbol{\mu})$	See (36)
Distribution to approximate J (8)	$\nu_\theta(\cdot \cdot, \cdot)$	$P(\cdot \boldsymbol{\theta}, \cdot, \cdot)$
Number of layers	L	5
MTG elements per layer	–	7
Number of GRU layers	–	2
Hidden size of each GRU layer	–	8
Dimension of $\boldsymbol{\theta}$	M	8448
Number of Monte Carlo samples to approximate (8)	–	15000
Integrator of the dynamics $\dot{\boldsymbol{\theta}}$ (7)	–	RK 5(4)
Offline GPU Training time	–	$\simeq 48\text{h}$
Burn-in length	–	3000
Length of the Markov chain	–	10000

Table 7: Computational setup, Normalizing Flow architecture, and parameter-sampling details for the Heston model (19).

C.1.1 Additional Numerical Experiments for the Heston Model

In Table 8, we report the relative error between the reference log-likelihood and the approximated log-likelihood, both at the true parameter $\boldsymbol{\mu}^*$ and averaged over a batch $\{\boldsymbol{\mu}^i\}_{i=1}^{N_{\text{test}}} \sim \hat{\pi}$ (cf. (36)) with $N_{\text{test}} = 100$, for NF and for the 2nd order closed-form expansions of Ait-Sahalia (A.-S.) [31] and the 4th order Itô-Taylor expansion [33]². The Fourier inversion of the characteristic function of the Heston model gives the reference. Among the benchmarked approximations, NF attains the smallest trajectory log-likelihood errors.

Table 8: Accuracy of the likelihood approximations for the Heston model (19). Best values in bold. The data are acquired with $\Delta = 0.5$.

Metric	NF	A.-S.	Itô-Taylor
Relative error over the log-lh (18) given $\boldsymbol{\mu}^*$	0.0003	0.0064	0.0093
Mean err. relative log-lh (18) given $\{\boldsymbol{\mu}^i\}_{i=1}^{N_{\text{test}}}$	0.063	0.401	0.361
Standard err. (mean err. relative log-lh)	0.012	0.078	0.089
Median err. relative log-lh (18) given $\{\boldsymbol{\mu}^i\}_{i=1}^{N_{\text{test}}}$	0.013	0.193	0.064

Table 9 presents a comparison of the performance of the approximated TPDF for sampling from the posterior distribution. NF achieves the shortest time per effective sample and the smallest empirical Wasserstein 2 distance in relation to the Fourier reference. To demonstrate the robustness of the

Table 9: Heston model (19). Runtime for 10^4 MCMC samples, empirical joint W_2 distance, and marginal parameter-wise W_2 distances relative to the Fourier reference. Best values in bold. A.-S. is omitted as it does not target the posterior.

Model	Method	Time (s)	W_2	W_2^α	W_2^β	W_2^σ	W_2^μ	W_2^ρ
Heston	Fourier	14560	Ref.	–	–	–	–	–
	NF	2243	0.066	0.0003	0.057	0.004	0.0046	0.0110
	Itô-Taylor	15069	0.948	0.0071	0.938	0.0918	0.0518	0.066

²Code for Ait-Sahalia’s expansion is publicly available at <https://www.princeton.edu/~yacine/research.htm>. At the time of our experiments, the implementation of [33] was available from the authors upon request.

Table 10: Heston model (19) with $\Delta = 0.5$; posterior means averaged across datasets, with pointwise 95% confidence intervals across datasets.

Parameter	True parameter μ^*	Fourier inversion	Normalizing Flow
α	0.10	0.1003 [0.0967, 0.1028]	0.1000 [0.0971, 0.1024]
β	3.00	3.087 [2.479, 3.596]	3.1279 [2.5684, 3.6564]
σ	0.25	0.2549 [0.2319, 0.2764]	0.2601 [0.2380, 0.2839]
μ	0.05	0.0479 [0.0229, 0.0761]	0.0565 [0.0303, 0.0859]
ρ	-0.80	-0.7977 [-0.8418, -0.7548]	-0.8135 [-0.8637, -0.7657]

likelihood profiles with respect to the simulated trajectory, we repeated the likelihood analysis on 25 independent datasets generated using the same μ^* , with all datasets supported on $\eta(x_0)$, i.e., contained in the support of the measure η . The resulting log-likelihood slices, along with pointwise confidence bands, are presented in Figure 4.

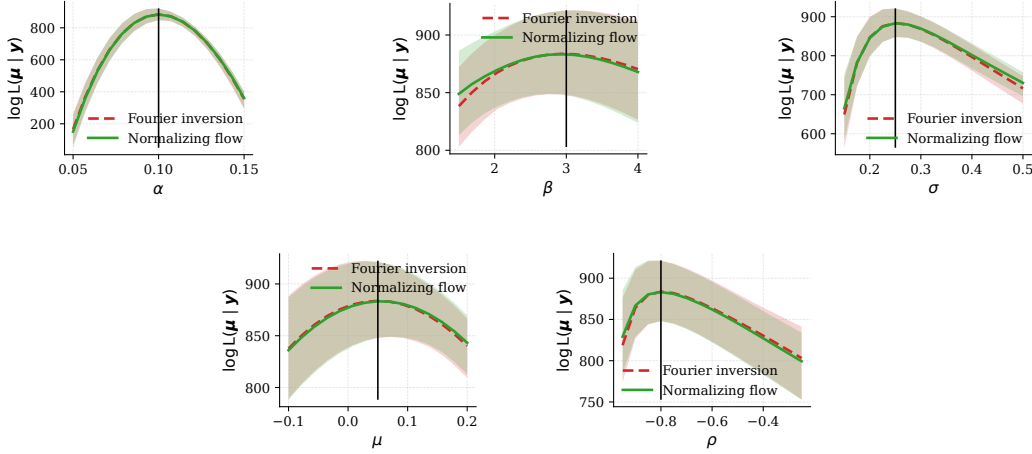


Figure 4: Log-likelihood profiles for the Heston model (19) with respect to each parameter, while fixing the others at their corresponding values of μ^* . The red dashed curves correspond to the semi-closed-form log-likelihood, and the green curves to the Normalizing Flow approximation. The black vertical line marks the true parameter value. The curves are computed over 25 independently generated datasets, and the shaded bands represent pointwise 95% confidence intervals across datasets. The sampling frequency is set to $\Delta = 0.5$.

We further evaluate the robustness of our model by using data sampled at a lower frequency, specifically with $\Delta = 1$ and $n + 1 = 200$. We integrate the dynamics (7) over the time interval $[0, \Delta]$ and conduct the same sensitivity analysis as shown in Figure 4. To achieve this, as done above, we generate 25 independent datasets and compute the likelihood profiles for each. The true parameter μ^* is fixed as in the previous experiments. The results are shown in Figure 5.

Our findings indicate that, in both observation regimes, our model qualitatively matches the width and shape of the confidence intervals produced by the semi-closed-form solution. This suggests that the Normalizing Flow is robust across various observation settings, supporting its use for Bayesian inference of diffusion processes.

We conduct a final test to evaluate the robustness of the model. Specifically, we generate 25 independent datasets $\{y^i\}_{i=1}^{25}$ with $\Delta = 0.5$, the same parameter μ^* and, for each of them, we run MCMC in the form of slice sampling to approximate the posterior distribution. We then compute the corresponding posterior means, and summarize these results across datasets. The comparison between the Fourier-based reference posterior and the Normalizing Flow approximation is presented in Table 10. Our results indicate that the posterior summaries obtained from Fourier inversion and the Normalizing Flow closely align for all parameters.

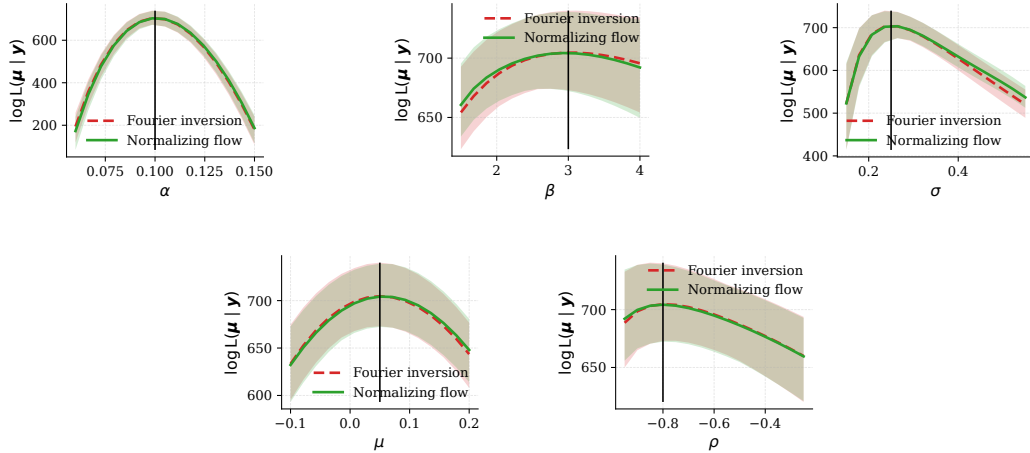


Figure 5: Log-likelihood profiles for the Heston model (19), obtained by varying one component of μ^* at a time while keeping the others fixed. The red dashed curves correspond to the semi-closed-form log-likelihood, and the green curves to the Normalizing Flow approximation. The black vertical line marks the true parameter value. The curves are computed over 25 independently generated datasets and the shaded bands represent pointwise 95% confidence intervals across datasets. The sampling frequency is set to $\Delta = 1$.

C.1.2 MCMC diagnostic for the Heston model

We diagnose the performance of the Flow-based MCMC sampler by investigating the chain’s mixing time. This indicator, as shown in Figure 6, is excellent.

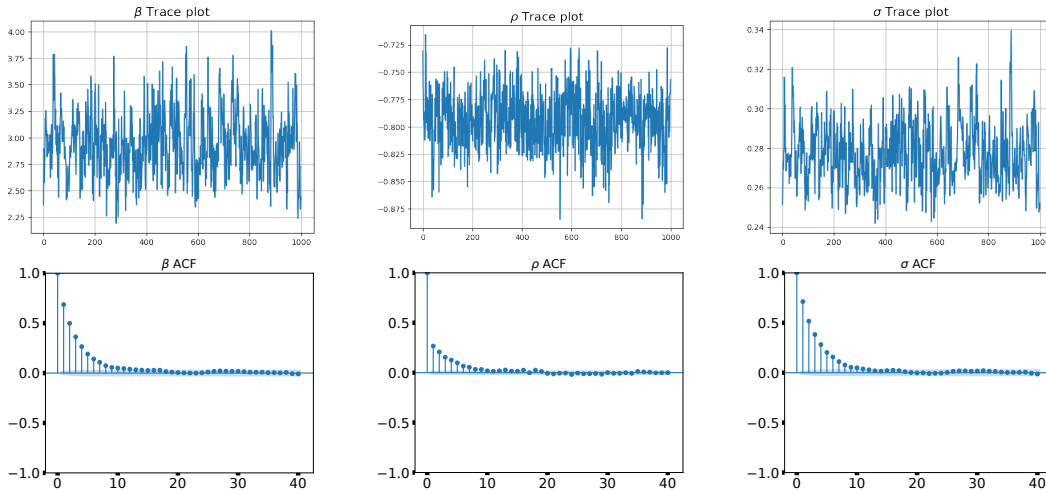


Figure 6: Trace plots and autocorrelation function for the parameters β , ρ and σ of the Heston model (19). The chain, drawn with MCMC in the form of axis-aligned, is composed of 10000 samples.

C.1.3 Additional Numerical Illustrations

In Figure 7, we report the marginal distribution of each parameter obtained by performing a Kernel Density plot on a chain of 10^4 samples. As visible in Figure 1, our model slightly overestimates the likelihood slice concerning the parameter ρ , and this effect is reflected in the corresponding posterior marginal distribution. The other posterior distributions show a close agreement.

Joint posterior plots for the Heston model, showing that the surrogate captures posterior correlations, are reported in Figure 8.

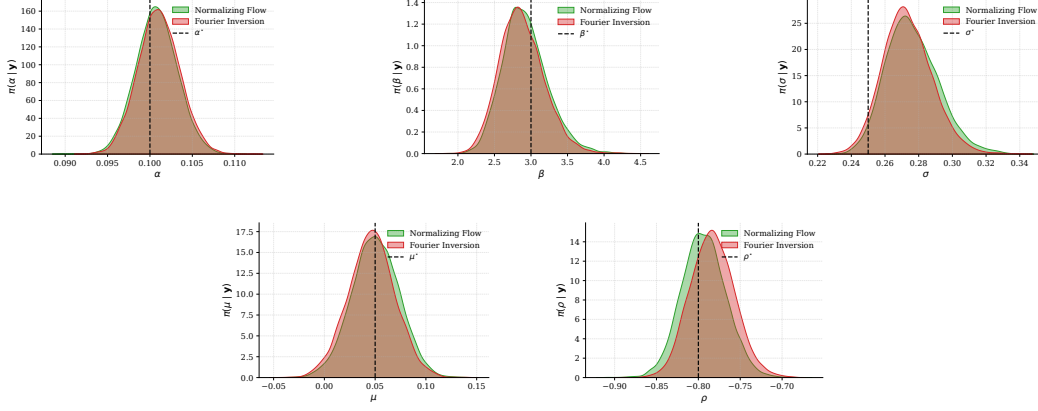


Figure 7: Posterior marginal distributions for the parameters of the Heston model (19).

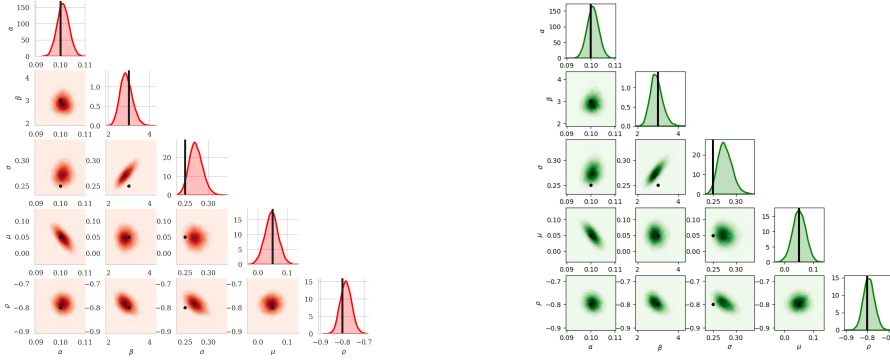


Figure 8: Samples drawn from the posterior distribution of the Heston model. In the left figure, the TPDF is obtained by Fourier inversion. In the right figure, the TPDF is approximated by Normalizing Flows.

D Setup for the SVCEV Stochastic Volatility Model

We describe the experimental setup for the SVCEV model. Using the same simulation strategy employed for the Heston model, we utilize the Euler-Maruyama scheme to simulate a trajectory consisting of $n + 1 = 100$ observations with parameters $\alpha^* = 0.1$, $\beta^* = 3$, $\sigma^* = 0.25$, $\mu^* = 0.05$, $\rho^* = -0.8$, $\gamma^* = 1$, $\Delta = 0.5$.

By conducting similar computations to those in [47], it can be shown that for $\gamma \in [0.5, 1]$ and $\sigma^2 \leq 2\alpha\beta$, the origin is inaccessible. This translates into a zero Dirichlet boundary condition in the FP equation $\rho(v = 0, y|t, 0, \mathbf{x}_0, \boldsymbol{\mu}) = 0$.

Setting $\mathbf{x} = (v, y)$, the FP equation associated with (20) reads

$$\begin{cases} \partial_t \rho(\mathbf{x}|t) + (\mu - v/2) \partial_y \rho(\mathbf{x}|t) + \beta(\alpha - v) \partial_v \rho(\mathbf{x}|t) - \beta \rho(\mathbf{x}|t) \\ - \frac{1}{2} \left(v \partial_y^2 \rho(\mathbf{x}|t) + \sigma^2 v^{2\gamma} \partial_v^2 \rho(\mathbf{x}|t) + 2\rho \sigma v^{\gamma+0.5} \partial_{vy}^2 \rho(\mathbf{x}|t) \right) \\ - \left(\gamma + \frac{1}{2} \right) \rho \sigma v^{\gamma-0.5} \partial_y \rho(\mathbf{x}|t) - 2\gamma \sigma^2 v^{2\gamma-1} \partial_v \rho(\mathbf{x}|t) \\ - \frac{1}{2} (2\gamma(2\gamma - 1) \sigma^2 v^{2(\gamma-1)}) \rho(\mathbf{x}|t) = 0 & (v, y) \in \mathbb{R}^+ \times \mathbb{R}, t \in (0, T], \\ \rho(v = 0, y|t, 0, \mathbf{x}_0, \boldsymbol{\mu}) = 0 & \text{for } y \in \mathbb{R}, t \in (0, T], \\ \rho(\mathbf{x}|0, 0, \mathbf{x}_0, \boldsymbol{\mu}) = \delta_{\mathbf{x}_0}(\mathbf{x}) & \text{for } (v, y) \in \mathbb{R}^+ \times \mathbb{R}, t \in \{0\}. \end{cases} \quad (37)$$

The determinant of the covariance matrix of the SVCEV model is given by $\det(\Sigma(t, v, y)) = \sigma^2 v^{2\gamma+1} (1 - \rho^2)$. This expression makes the solution of (37) more challenging than in the affine case where $\gamma = 0.5$, as the determinant approaches zero at a rate that increases with γ .

The TPDF is decomposed as done for the Heston model (31); the map \mathbf{n}_θ updates the volatility independently while conditioning the asset price on it. To approximate the Neural Galerkin residual (8), we choose $\eta(\mathbf{x}_0)$ as

$$\eta(\mathbf{x}_0) = \mathcal{U}(v_0; [0, 0.25])\mathcal{U}(y_0; [-4, 3]). \quad (38)$$

The distribution $\tilde{\pi}_0$ is chosen as

$$\begin{aligned} \tilde{\pi}_0(\boldsymbol{\mu}) = & 1_{\{\alpha>0\}}\phi(\alpha|0.1, 0.08)1_{\{\beta>0\}}\phi(\beta|3, 0.2) \times \\ & 1_{\{\sigma \in (0, \sqrt{2\alpha\beta}]\}}\phi(\sigma|0.25, 0.08)\phi(\mu|0.05, 0.03)1_{\{-1 \leq \rho \leq 1\}}\phi(\rho| - 0.8, 0.08) \times \\ & 1_{\{0.5 \leq \gamma \leq 1\}}\phi(\gamma|1, 0.2). \end{aligned} \quad (39)$$

while the prior is set as

$$\pi_0(\boldsymbol{\mu}) = 1_{\{\alpha>0\}}1_{\{\beta>0\}}1_{\{\sigma \in (0, \sqrt{2\alpha\beta}]\}}1_{\{-1 \leq \rho \leq 1\}}1_{\{0.5 \leq \gamma \leq 1\}}. \quad (40)$$

The reference distribution of the Normalizing Flow is set as for the Heston model (see section C). The linear scaling defined in (32) is used to map the variables into $[0, 1]^d$ prior to applying the reference distributions.

Instead of solving for (37), we found it more stable to solve the PDE for the log-density: $q(\mathbf{x}|\boldsymbol{\theta}(\tau), \mathbf{x}_0, \boldsymbol{\mu}) = \log(\mathbb{P}(\mathbf{x}|\boldsymbol{\theta}(\tau), \mathbf{x}_0, \boldsymbol{\mu}))$. The increased stability we achieve is related to the fast decay of the initial condition, which, after the log-transformation, becomes more manageable.

At inference time, in Table 4, we test the model on the distribution

$$\begin{aligned} \hat{\pi}(\boldsymbol{\mu}) = & 1_{\{\alpha>0\}}\phi(\alpha|0.1, 0.03)1_{\{\beta>0\}}\phi(\beta|3, 0.2) \times \\ & 1_{\{\sigma \in (0, \sqrt{2\alpha\beta}]\}}\phi(\sigma|0.25, 0.03)\phi(\mu|0.05, 0.03)1_{\{-1 \leq \rho \leq 1\}}\phi(\rho| - 0.8, 0.07) \times \\ & 1_{\{0.5 \leq \gamma \leq 1\}}\phi(\gamma|1, 0.2). \end{aligned} \quad (41)$$

The remaining computational parameters and training details are reported in Table 11.

Quantity	Symbol	Value
Diffusion domain	Ω	$\mathbb{R}^+ \times \mathbb{R}$
Parameter of the support of the NF (Volatility)	$[\hat{a}_1, \hat{b}_1]$	[0,3]
Parameter of the support of the NF (log-Asset)	$[\hat{a}_2, \hat{b}_2]$	[-6.5,6.5]
Initial condition distribution	$\eta(v_0, y_0)$	See (38)
Parameter training distribution	$\tilde{\pi}_0(\boldsymbol{\mu})$	See (39)
Parameter test distribution	$\hat{\pi}(\boldsymbol{\mu})$	See (41)
Distribution to approximate J (8)	$\nu_\theta(\cdot \cdot, \cdot)$	$\mathbb{P}(\cdot \boldsymbol{\theta}, \cdot, \cdot)$
Number of Neural Galerkin samples	N	8066
Number of layers	L	5
MTG elements per layer	–	4
Number of GRU layers	–	4
Hidden size of each GRU layer	–	5
Dimension of $\boldsymbol{\theta}$	M	6756
Number of Monte Carlo samples to approximate (8)	–	13512
Integrator of the dynamics $\dot{\boldsymbol{\theta}}$ (7)	–	RK 5(4)
Offline GPU Training time	–	$\simeq 48\text{h}$
Burn-in length	–	3000
Length of the Markov chain	–	10000

Table 11: Computational setup, Normalizing Flow architecture, and parameter-sampling details for the SVCEV model (20).

D.1 Validation of the reference benchmark for the SVCEV Model

We validate the accuracy of the data augmentation strategy used to benchmark the SVCEV model. The core idea of this strategy is to insert $\hat{M} - 1$ latent variables between two physical observations

and then integrate them out to express the TPDF as follows:

$$p(\mathbf{y}_{t_i} | \Delta, \mathbf{y}_{t_{i-1}}, \boldsymbol{\mu}) = \int \prod_{m=0}^{\hat{M}-1} p(\mathbf{u}_{m+1} | \Delta / \hat{M}, \mathbf{u}_m, \boldsymbol{\mu}) d\mathbf{u}_1, \dots, \mathbf{u}_{\hat{M}-1}, \quad (42)$$

where $\mathbf{u}_0 = \mathbf{y}_{t_{i-1}}$ and $\mathbf{u}_{\hat{M}} = \mathbf{y}_{t_i}$. The integral in (42) is not computable in general. Still, since the observation frequency has been increased by a factor \hat{M} , each term $p(\mathbf{u}_{m+1} | \Delta / \hat{M}, \mathbf{u}_m, \boldsymbol{\mu})$ can be approximated using the Euler-Maruyama TPDF. The integral can then be evaluated using Importance Sampling. The choice of the importance measure has been discussed in [45]. We use the so-called Modified Brownian Bridge (MBB); see p. 305 of [45]. Each term of the likelihood function is evaluated by sampling N_{MC} independent realizations of the Modified Brownian Bridge and by approximating (42) by its Monte Carlo estimator

$$p(\mathbf{y}_{t_i} | \Delta, \mathbf{y}_{t_{i-1}}, \boldsymbol{\mu}) \simeq \frac{1}{N_{MC}} \sum_{k=1}^{N_{MC}} \frac{\prod_{m=0}^{\hat{M}-1} \phi(\mathbf{u}_{k,m+1} | \Delta / \hat{M}, \mathbf{u}_{k,m}, \boldsymbol{\mu})}{\prod_{m=0}^{\hat{M}-2} q(\mathbf{u}_{k,m+1} | \Delta / \hat{M}, \mathbf{u}_{k,m}, \boldsymbol{\mu})}, \quad (43)$$

where ϕ denotes the TPDF associated with the Euler-Maruyama scheme with timestep size Δ / \hat{M} and q denotes the importance measure.

We estimate the likelihood (18) as

$$\hat{\mathbb{L}}(\boldsymbol{\mu} | \mathbf{y}) = \prod_{i=1}^n \frac{1}{N_{MC}} \sum_{k=1}^{N_{MC}} \frac{\prod_{m=0}^{\hat{M}-1} \phi(\mathbf{u}_{i,k,m+1} | \Delta / \hat{M}, \mathbf{u}_{i,k,m}, \boldsymbol{\mu})}{\prod_{m=0}^{\hat{M}-2} q(\mathbf{u}_{i,k,m+1} | \Delta / \hat{M}, \mathbf{u}_{i,k,m}, \boldsymbol{\mu})}. \quad (44)$$

To assess the accuracy of the data-augmentation likelihood estimator, we compare coarser resolutions (\hat{M}, N_{MC}) against a reference estimate $\hat{\ell}_{\text{ref}}$ obtained using the same estimator at a finer discretization, namely $(\hat{M}, N_{MC}) = (1500, 3000)$. Starting from this reference resolution, we then evaluate additional estimators generated by successively halving both \hat{M} and N_{MC} , including $(\hat{M}, N_{MC}) = (1000, 2500)$. Table 12 shows that the relative errors at the finest resolutions are on the order of 10^{-4} , and that the estimators tend to converge toward the reference value.

In light of these results, to get a reference for the experiments in Table 4, we employ $\hat{M} = 1000$ and $N_{MC} = 2500$, leading to $\Delta / \hat{M} = 5 \times 10^{-4}$. Instead, to keep the cost of the MCMC experiment in section 6.2 affordable, we sample the reference chain with $M = 200$ and $N = 400$.

\hat{M}	N_{MC}	$\hat{\ell}(\hat{M}, N_{MC})$	Relative error	95% CI (rel. error)
1000	2500	368.979	5.46×10^{-4}	$[4.96, 5.96] \times 10^{-4}$
750	1500	368.972	7.17×10^{-4}	$[6.50, 7.84] \times 10^{-4}$
375	750	368.927	1.018×10^{-3}	$[9.20, 11.17] \times 10^{-4}$
187	375	368.772	1.409×10^{-3}	$[1.273, 1.546] \times 10^{-3}$
93	187	368.576	2.082×10^{-3}	$[1.885, 2.279] \times 10^{-3}$
46	93	367.986	3.504×10^{-3}	$[3.177, 3.831] \times 10^{-3}$

Table 12: Validation results for the data-augmentation likelihood estimator. The table reports the estimated log-likelihood, the relative error over the log-likelihood, and the corresponding 95% confidence interval for the relative error. The confidence intervals are constructed by repeating the simulation 250 times.

E Three-factor short rate model

We further validate the scalability of our surrogate model by considering the time-homogeneous trivariate BDFS model, as introduced in [50]. The BDFS is an extension of the univariate short rate model, incorporating both a stochastic long-run mean and a stochastic volatility. The long-run mean is modeled by an Ornstein-Uhlenbeck (OU) process, while a CIR process describes the volatility.

This model is irreducible and reads

$$\begin{cases} dV(t) = k_1(\alpha_1 - V(t))dt + \sigma_1\sqrt{V(t)}dW_1(t) \\ dO(t) = k_2(\alpha_2 - O(t))dt + \sigma_2dW_2(t) \\ dY(t) = k_3(O(t) - Y(t))dt + \sqrt{V(t)}(\rho dW_1(t) + \sqrt{1 - \rho^2}dW_3(t)) \\ V(0) = v_0, O(0) = o_0, Y(0) = y_0, \end{cases} \quad (45)$$

where $W_1(t)$, $W_2(t)$ and $W_3(t)$ are three independent Brownian motions.

We simulate a trajectory of length $n + 1 = 350$ with $\Delta = 0.5$ from (45) using the same strategy as for (19): we introduce 5000 sub-intervals per sampling interval and discard 4999 of them. We generate 700 observations and drop the first 350. We use the following parameters $k_1 = 3$, $\alpha_1 = 0.1$, $\sigma_1 = 0.25$, $k_2 = 7$, $\alpha_2 = 0.06$, $\sigma_2 = 0.03$, $k_3 = 10$, $\rho = 0.5$, which we denote by $\boldsymbol{\mu}^* \in \mathbb{R}^8$. Thus, the residual in equation (8) is minimized over an $8 + 3 + 3 = 14$ dimensional space.

Denoting with $\boldsymbol{x} = [v, o, y]$, the Fokker Planck equation associated with (45) is

$$\begin{cases} \partial_t \rho(\boldsymbol{x}|t) + k_3(o - y)\partial_y \rho(\boldsymbol{x}|t) \\ + k_2(\alpha_2 - o)\partial_o \rho(\boldsymbol{x}|t) + k_1(\alpha_1 - v)\partial_v \rho(\boldsymbol{x}|t) \\ - (k_1 + k_2 + k_3)\rho(\boldsymbol{x}|t) \\ - \frac{1}{2} [v\partial_y^2 \rho(\boldsymbol{x}|t) + \sigma_2^2 \partial_o^2 \rho(\boldsymbol{x}|t) + \sigma_1^2 v \partial_v^2 \rho(\boldsymbol{x}|t) \\ + 2\rho\sigma_1 v \partial_{yv}^2 \rho(\boldsymbol{x}|t)] - (\rho\sigma_1 \partial_y \rho(\boldsymbol{x}|t) \\ + \sigma_1^2 \partial_v \rho(\boldsymbol{x}|t)) = 0 & \text{for } (v, o, y) \in \mathbb{R}^+ \times \mathbb{R} \times \mathbb{R}, t \in (0, T], \\ \rho(v = 0, o, y|t, 0, \boldsymbol{x}_0, \boldsymbol{\mu}) = 0 & \text{for } (o, y) \in \mathbb{R} \times \mathbb{R}, t \in (0, T], \\ \rho(\boldsymbol{x}|0, 0, \boldsymbol{x}_0, \boldsymbol{\mu}) = \delta_{\boldsymbol{x}_0}(\boldsymbol{x}) & \text{for } (v, o, y) \in \mathbb{R}^+ \times \mathbb{R} \times \mathbb{R}, t \in \{0\}. \end{cases} \quad (46)$$

We utilize a flat prior restricted to the parameters' domain

$$\pi_0(\boldsymbol{\mu}) = \mathbb{1}_{\{\alpha_1 > 0\}} \mathbb{1}_{\{k_1 > 0\}} \mathbb{1}_{\{\sigma_1 \in (0, \sqrt{2\alpha_1 k_1})\}} \mathbb{1}_{\{\alpha_2 > 0\}} \mathbb{1}_{\{k_2 > 0\}} \mathbb{1}_{\{\sigma_2 > 0\}} \mathbb{1}_{\{k_3 > 0\}} \mathbb{1}_{\{-1 \leq \rho \leq 1\}}, \quad (47)$$

and, for the training phase, we sample the parameters $\boldsymbol{\mu}$ by implicitly specifying $\tilde{\pi}_0$ as

$$\begin{cases} k_1 \sim \mathcal{U}(\cdot; [1.5, 4]), \\ \alpha_1 \sim \mathcal{U}(\cdot; [0.005, 0.25]), \\ \sigma_1 \sim \mathcal{U}(\cdot; [0.05, 0.4]), \\ k_2 \sim \mathcal{U}(\cdot; [4, 10]), \\ \alpha_2 \sim \mathcal{U}(\cdot; [-1.5, 0.25]), \\ \sigma_2 \sim \mathcal{U}(\cdot; [10^{-3}, 0.25]), \\ k_3 \sim \mathcal{U}(\cdot; [7.5, 13]), \\ \rho \sim \mathcal{U}(\cdot; [0.1, 0.9]), \end{cases} \quad (48)$$

where $\mathcal{U}(\cdot; [a, b])$ denotes the uniform distribution over the interval $[a, b]$. Samples from $\tilde{\pi}_0$ are further restricted to the prior's support.

We set the distribution of the initial condition as

$$\eta(\boldsymbol{x}_0) = \mathcal{U}(v_0; [0, 0.75])\mathcal{U}(o_0; [-2.5, 2.5])\mathcal{U}(y_0; [-2.5, 2.5]). \quad (49)$$

where $\boldsymbol{x}_0 = [v_0, o_0, y_0]$.

Like the decomposition of the TPDF of the Heston model (31), we can also decompose the TPDF of the BDFS model as

$$p_{V,O,Y}(v, o, y|v_0, o_0, y_0) = p_V(v|v_0, o_0, y_0)p_O(o|v_0, o_0, y_0)p_{Y|V,O}(y|v, o, v_0, o_0, y_0). \quad (50)$$

The transport map $\boldsymbol{n}_\theta(v, o, y)$ is constructed so that the volatility v and the long term-mean o are updated independently from all the other variables. At the same time, the asset price y is modified by conditioning on v and o (which implies setting $m = 2$ in the architecture of the Normalizing Flow).

The reference distribution is picked as a uniform distribution over $[0, 1]$ for the components of the transport map related to o and y , while a Gamma distribution truncated over $[0, 1]$ serves as the reference density for the first component of \boldsymbol{n}_θ . The linear scaling defined in equation (32) is used to map the variables into the range $[0, 1]^d$ before applying the reference distributions.

The computational parameters and training details are summarized in Table 13.

Quantity	Symbol	Value
Diffusion domain	Ω	$\mathbb{R}^+ \times \mathbb{R} \times \mathbb{R}$
Parameter of the support of the NF (Volatility)	$[\hat{a}_1, \hat{b}_1]$	[0,2]
Parameter of the support of the NF (OU process)	$[\hat{a}_2, \hat{b}_2]$	[-3,3]
Parameter of the support of the NF (log-Asset)	$[\hat{a}_3, \hat{b}_3]$	[-3,3]
Initial condition distribution	$\eta(\mathbf{x}_0)$	See (49)
Parameter distribution	$\tilde{\pi}_0(\boldsymbol{\mu})$	See (48)
Distribution to approximate J (8)	$\nu_\theta(\cdot \cdot, \cdot)$	$P(\cdot \boldsymbol{\theta}, \cdot, \cdot)$
Number of layers	L	5 (Process Y) and 4 (O, V)
MTG elements per layer	–	5 for $l > 2$
Number of GRU layers	–	4
Hidden size of each GRU layer	–	8 (Process Y) and 6 (O, V)
Dimension of $\boldsymbol{\theta}$	M	14448
Number of Monte Carlo samples to approximate (8)	–	17338
Integrator of the dynamics $\dot{\boldsymbol{\theta}}$ (7)	–	RK 5(4)
Offline GPU Training time	–	$\simeq 54$ h
Burn-in length	–	3000
Length of the Markov chain	–	10000

Table 13: Computational setup, Normalizing Flow architecture, and parameter-sampling details for the BDFS model (45).

E.0.1 Log-likelihood and posterior analysis

In Figure 9, we show how the log-likelihood varies with respect to each parameter (having fixed all the others to the true values of $\boldsymbol{\mu}^*$). We compare our Normalizing Flow against a saddlepoint approximation derived from the explicitly available characteristic function (see, e.g., [51]). Our results show good agreement, suggesting that our Normalizing Flow model is a promising surrogate, even in high-dimensional settings.

Finally, we draw samples from the posterior distribution using MCMC in the form of Slice Sampling with axis-aligned. For this example, we do not compare the NF’s performance to any reference, as targeting the posterior via the saddlepoint approximation proved computationally intractable. The marginal posterior distributions, presented in Figure 10, assign meaningful uncertainty to the model’s parameters, indicating that the Normalizing Flow appears scalable to higher-dimensional benchmarks.

F Sampling from the Truncated-bounded Normalizing Flow

In general, when there are multiple elements in the mixture of Gaussians (12), we lose the analytic invertibility of n_θ , and sampling from (10) requires the solution of nonlinear equations. We consider two alternatives for sampling from the Normalizing Flow: a high-fidelity root-finding method and an approximate method that is computationally cheaper. Here, we approximate the target density P by replacing the bijection of layer l , for $l \geq 2$, with the CDF of a unique element of the mixture of truncated Gaussian random variables. This element is chosen with probability given by its mixture weight. The entire procedure is reported in Algorithm 2. We remark that the parameters \mathbf{x}_0 and $\boldsymbol{\mu}$ influence the sampling step, as they define the mean, variances, and mixture weight characterizing the mixture of Gaussians of each layer.

The approximate method is not designed to replicate the exact sampler with arbitrary precision, but rather to generate representative training points at a much lower computational cost. Since it is solely employed to generate samples for evaluating the training residual, it does not need to be exact. During testing, to obtain more reliable samples from the model, root-finding routines can be implemented instead.

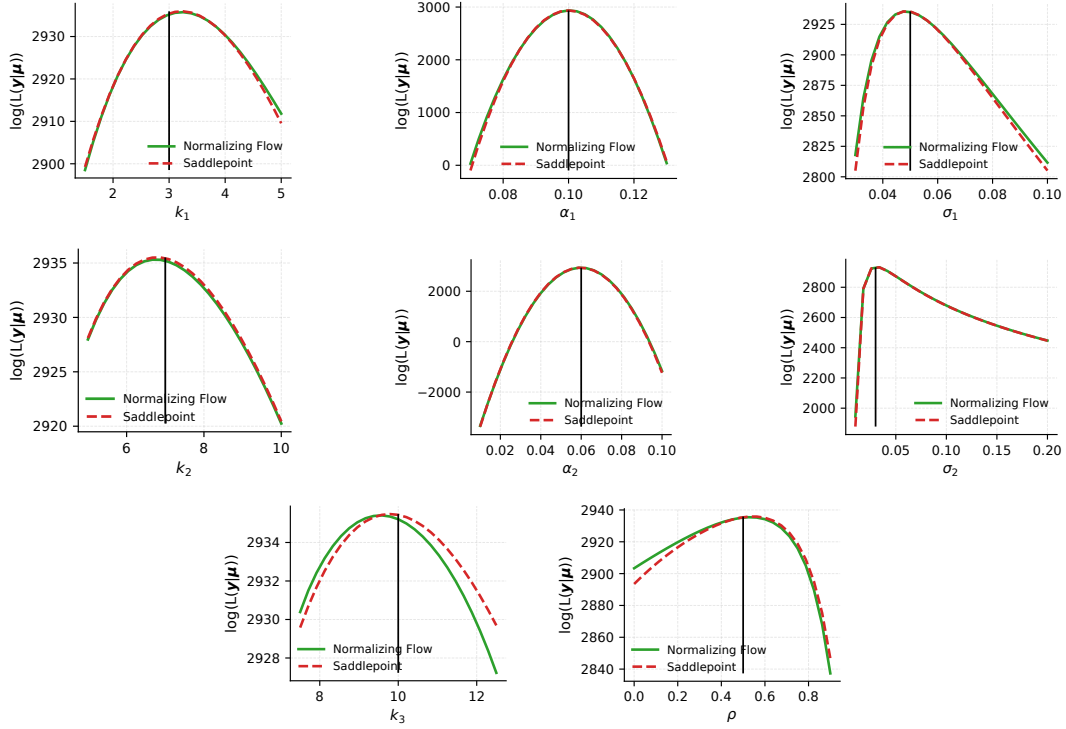


Figure 9: Log-likelihood evaluated on data generated from the BDFS model (45) with parameter $\boldsymbol{\mu}^*$, varying one component of $\boldsymbol{\mu}^*$ at a time. The different plots show the dependence on each parameter when the others are fixed to the true value of $\boldsymbol{\mu}^*$. The log-likelihood computed via saddlepoint approximation is depicted with red dashed lines, while the log-likelihood approximated by the Normalizing Flow is shown in green. A vertical line centered on the true parameter is shown in black.

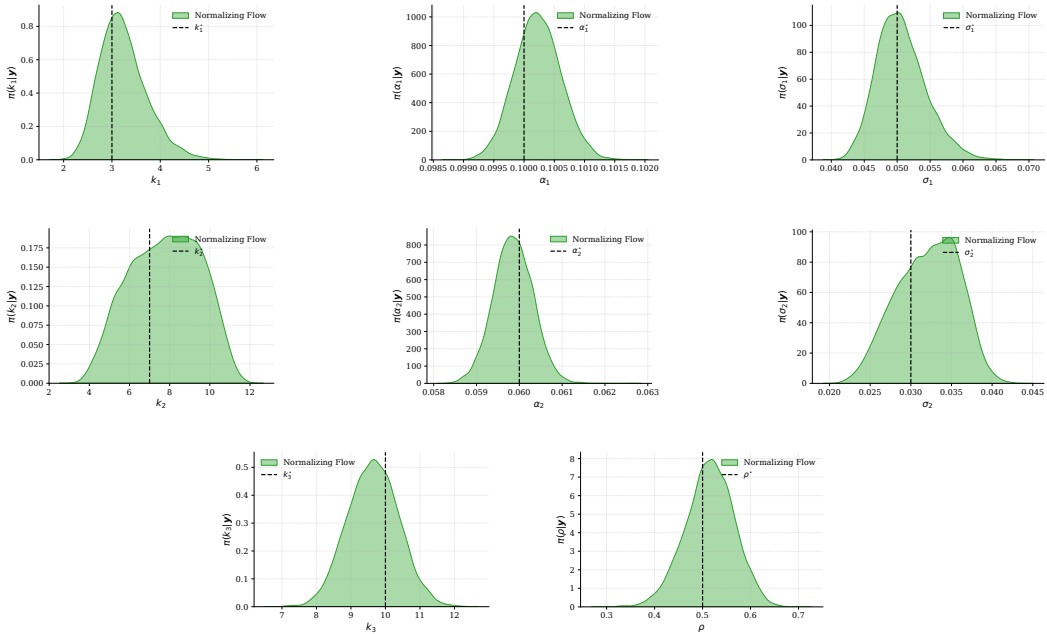


Figure 10: Posterior marginal distributions for the parameters of the BDFS model (45). The chain is composed of 10000 samples.

Algorithm 2 Sampling from $P(\cdot | \theta(\tau), \mathbf{x}_0, \boldsymbol{\mu})$

Require: τ : relative time instant of the Normalizing Flow; \mathbf{x}_0 ; $\boldsymbol{\mu}$

Ensure: Sample $\mathbf{x} \sim P(\cdot | \theta(\tau), \mathbf{x}_0, \boldsymbol{\mu})$

```
1:  $z^L \sim \mathcal{Z}$  ▷ Draw a sample from the reference distribution
2: for  $m = 0, \dots, d - 1$  do
3:   for  $l = L, \dots, 2$  do
4:      $\tilde{z}_{m+1}^l = \frac{z_{m+1}^l + 1}{2}$ 
5:      $[\boldsymbol{\alpha}^{l,m+1}(\tau), \mathbf{m}^{l,m+1}(\tau), \boldsymbol{\sigma}^{l,m+1}(\tau)] = \text{NN}^{l,m+1}(\mathbf{x}_{1:m}, \mathbf{x}_0, \boldsymbol{\mu})$  ▷ Compute the parameters of the MTG
6:     if Exact Sampling then
7:       Solve for  $z_{m+1}^{l-1}$  in
          
$$\tilde{z}_{m+1}^l = \sum_{k=1}^{G_{l,m+1}} \alpha_k^{l,m+1}(\tau) \Phi \left( z_{m+1}^{l-1} \mid \mathbf{m}_k^{l,m+1}(\tau), \sigma_k^{l,m+1}(\tau), -1, 1 \right)$$

          using a root-finding algorithm
8:     else
9:        $k \sim \mathcal{A}(\cdot | \boldsymbol{\alpha}^{l,m+1})$  ▷ Select one index from the discrete distribution on  $\{1, \dots, G_{l,m+1}\}$ 
10:       $z_{m+1}^{l-1} = \Phi^{-1} \left( \tilde{z}_{m+1}^l \mid \mathbf{m}_k^{l,m+1}, \sigma_k^{l,m+1}, -1, 1 \right)$  ▷ Analytical inversion of the selected truncated Gaussian CDF
11:    end if
12:  end for
13:   $x_{m+1} = \frac{z_{m+1}^1 + 1}{2} (\hat{b}_{m+1} - \hat{a}_{m+1}) + \hat{a}_{m+1}$  ▷ Rescale the sample to the NF's support  $[\hat{a}_{m+1}, \hat{b}_{m+1}]$ 
14: end for
15: return  $\mathbf{x}$ 
```

F.1 Approximated sampling from Normalizing Flows: validation

We will empirically evaluate whether the approximate samples generated by Algorithm 2 are sufficiently representative to serve as training points for estimating the expected residual. Our validation procedure consists of two main steps:

- After the training phase, given a prescribed initial condition $\mathbf{x}_0 \sim \eta$, parameter vector $\boldsymbol{\mu} \sim \tilde{\pi}_0$, and time horizon Δ , we use Algorithm 2 to obtain N samples from the Normalizing Flow.
- We push these samples back through the Normalizing Flow using the map \mathbf{n}_{θ^*} and check whether their distribution aligns with the Normalizing Flow's reference distribution.

To maintain a moderately high-dimensional framework, we conduct this validation phase on the Normalizing Flow trained on the model described in section E. This test assesses whether the map correctly transforms the samples into the intended reference distribution of the Normalizing Flow. We consider the third component of the transport map, which approximates the conditional distribution of the log-asset price, namely a uniform distribution over $[0, 1]$.

We draw 400 samples from the Normalizing Flow conditioned on the following parameters: $\boldsymbol{\mu} = \boldsymbol{\mu}^*$ and $\mathbf{x}_0 = [0.0948, 0.0559, -0.013]$. We consider a time horizon of $\Delta = 0.05$, which is a crucial moment for the optimization routine because the intensity of the singular initial condition is still very concentrated. In the early stages of the optimization process, it is essential to obtain sufficiently representative samples to evaluate the expected residual stably.

We conduct the same test using a high-fidelity Bisection method, which effectively approximates the inverse of the transport map \mathbf{n}_{θ} within a specified tolerance. In Figure 11, we compare the quantiles

obtained by the two methods. We also repeat the test at a later time, $\Delta = 0.5$, which occurs at the conclusion of the optimization routine. The results for this test are illustrated in Figure 12.

The quantiles reconstructed using our algorithm exhibit greater deviation from the reference distribution than those obtained with the Bisection method. However, the computational effort required to run Algorithm 2 is significantly lower, especially when aiming for very small tolerances with the root-finding algorithm. As previously mentioned, our algorithm does not need to be exact within a specific tolerance; instead, it aims to provide samples that represent the general behavior of the reference distribution. As illustrated in Figures 11 and 12, the quantiles derived from our approximated algorithm align reasonably well with the true quantiles. Although we do not investigate this point further here, using samples close to the support of the true distribution, but not necessarily sampled from it, may be beneficial for estimating the expected residual. Indeed, they may act as contrastive samples, preventing the numerical solution from collapsing onto the training points. This collapse could occur because the null solution minimizes the residual linked to the Fokker-Planck equation. This sampling strategy can be further refined using speculative sampling techniques [52]. By selecting a simplified target architecture with only one Gaussian per layer as a draft model, we can accept or reject its proposals to draw exact samples from the Normalizing Flow at a significantly lower cost.

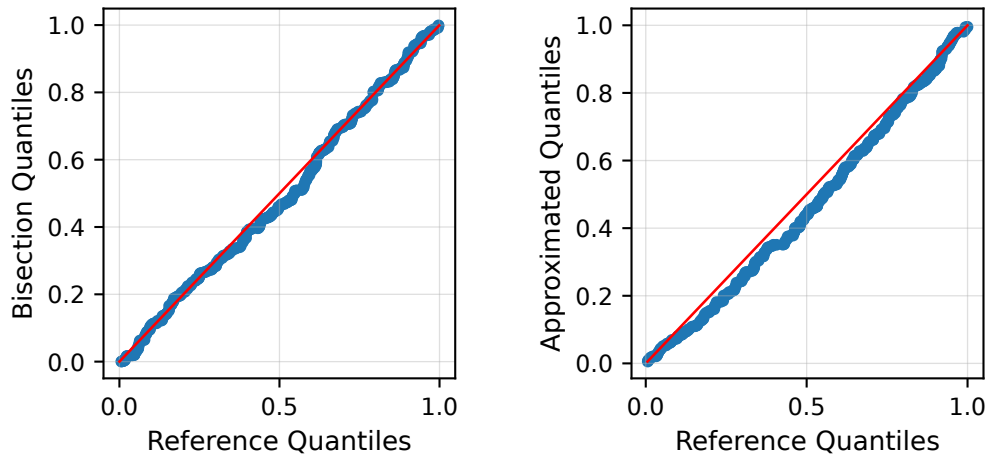


Figure 11: Q-Q (quantile-quantile) plot comparing the reference distribution of the conditional density of the log-asset price approximated with the Bisection-Method (left) and with Algorithm 2 (right). The Normalizing Flow is parametrized by the weights and biases saved at time 0.05 of Algorithm 1.

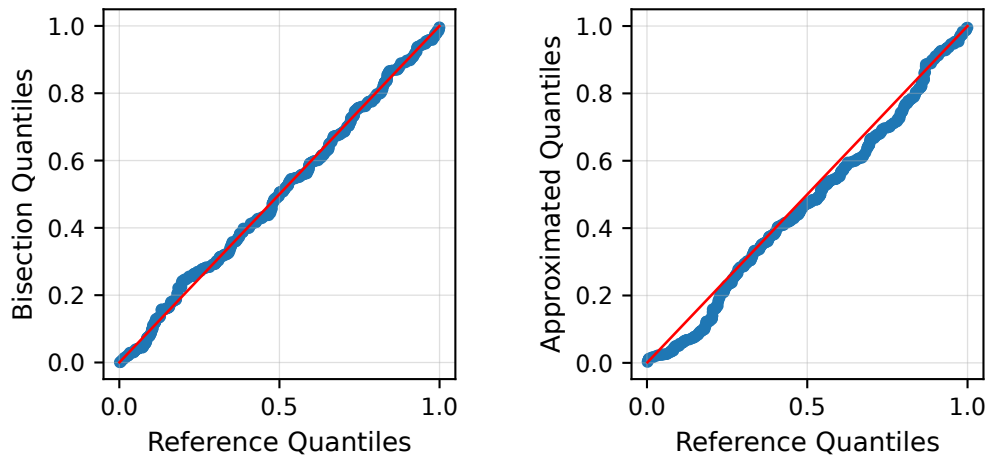


Figure 12: Q-Q (quantile-quantile) plot comparing the reference distribution of the conditional density of the log-asset price approximated with the Bisection-Method (left) and with Algorithm 2 (right). The Normalizing Flow is parametrized by the weights and biases saved at time 0.5 of Algorithm 1.